# IISc Theses Abstracts

## Contents

*J. Indian Inst. Sci.*, May–June 1993, **73**, 261–312

# IISc THESES ABSTRACTS

Thesis Abstract (Ph.D.)

## Analytic and numerical studies of neural network models of associative memory by

Varsha Deshpande.
Research supervisor: Chandan Dasgupta.
Department: Physics.

### 1. Introduction

Recently, a lot of interest has been focused on neural network models of content addressable memory. A neural network is a large, highly connected assembly of simple computing elements (neurons). In the simplest models, each neuron is assumed to be a two-state threshold device having outputs +1 or −1, representing the active or the quiescent state, respectively. Such a neuron may be represented by an Ising spin. The information (memories) stored in the network is embedded in the interconnections (synaptic efficacies) among the neurons. The time evolution of the network is governed by an assumed dynamics of the individual neurons. The system behaves like a content-addressable memory if the configurations representing the stored memories are locally stable attractors of the assumed dynamics.

The neural network models which have received the greatest attention from physicists belong to a class of which the original Hopfield model[1,2] is the simplest example. In these models, the synaptic interaction matrix is assumed to be symmetric with zero as diagonal elements. One may then define an 'energy function' (Hamiltonian) for the network which has the property that the most commonly assumed dynamics of the neurons corresponds to the rule that the state of a neuron is changed (the corresponding Ising spin is flipped) only if the energy is decreased in the process. Such a network functions as a content addressable memory if the interaction matrix is chosen so as to make the memorized configurations local minima of the associated energy function. This analogy with a spin system described by a Hamiltonian has made possible the application of many concepts and techniques developed in the statistical mechanics of disordered spin systems to the study of neural networks. In the original Hopfield model, the memories were assumed to be random binary strings (strings of elements each of which take on the values +1 and −1 with equal probability) and the so-called 'generalized Hebb rule' was used to construct the synaptic matrix. Extensive studies[3,4] using methods of statistical mechanics have shown that this model functions as an associative memory if the number of stored memories does not exceed about 15% of the total number of neurons. This restriction on the storage capacity is a major shortcoming of the Hopfield model. Another problem with the Hopfield model arises from the fact that it performs very poorly if the patterns to be stored have strong correlations among themselves. In this work, we have constructed a number of alternate models of associative memory and studied the behaviour of these models by using analytic and numerical techniques.

### 2. Hierarchical models for storing correlated memories

During the last few years, several attempts have been made to overcome the shortcomings of the Hopfield model. In particular, several neural network models with a hierarchical organization of correlated memories have been proposed. We consider a class of hierarchical neural network models introduced by Dotsenko[5,6] for the storage and associative recall of strongly correlated memories. In these models, patterns stored in higher levels of the hierarchy represent generalized categories and those stored in lower levels describe finer details We first show that the models originally proposed by Dotsenko have a serious flaw: they are not able to detect or correct errors in categorization which may be present in the input, if, as originally proposed, the patterns stored in the lower levels correspond to random binary strings. We then describe, two different models which attempt to overcome this shortcoming of the original models. We show that if the interaction between different levels of hierarchy is taken, as suggested by Dotsenko, to have the form of a uniform field acting on the lower-level spins, then the system cannot correct any error in categorization. This is due to the fact that the energy associated with the uniform field term is much less than that of the Hopfield term which, as a result, is dominant. To overcome the problem, we redefine the interactions between two levels of hierarchy to have the form of a field conjugate to memories stored in the lower level. In the second model, a three-spin interaction term is included in the lower level in addition to the usual binary interactions of the Hopfield type The inclusion of such a term breaks the symmetry between a memory and its complement state and helps in correcting errors in categorization in the lower level of hierarchy. Detailed analytical and numerical studies of the performance of these models are presented. In the analytic calculations, we make extensive use of concepts and techniques of statistical mechanics. Our analysis shows that both these models are able to detect and also to correct in varying degrees any error in categorization that may be present in the input pattern.

### 3. Models for storing individual patterns in limit cycles

The models described above use attractive fixed points of the underlying dynamics to store and retrieve memories. A general dynamical system with many interacting variables may, of course, exhibit stable attractors other than fixed points. We have, therefore, studied neural network models which use limit cycles for carrying out specific tasks. In these models, there are two kinds of interactions: a Hopfield-like term that tends to stabilize the system in a memorized state and a second term with a time delay that acts to induce transitions between a memorized state and its complement state. For a proper choice of the values of the parameters, this model exhibits limit-cycle behaviour in which the overlap with a target pattern oscillates in time with a large amplitude and overlaps with all the other stored patterns remain close to zero. An asymmetrically diluted version of the model is solved exactly in the limit of extreme dilution. We find that the model with cycles performs better than a similarly diluted version of the Hopfield model. The performance of the fully connected model is studied by numerical simulations. We find a behaviour qualitatively similar to that of the dilute model. The model with cycles is found to perform better than the Hopfield model as a pattern classifier if the memory loading level and the degree of corruption of the input patterns are large.

We have also used the principles of the model with limit cycles to construct a third model for hierarchical storage of correlated memories. This model makes use of a set of interactions with a time delay to induce, if necessary, transitions between memory states and their complements to correct any error in categorization which may be present in the input state. Numerical simulations show that this model performs as desired.

**References**

| | |
|---|---|
| 1. Hopfield, J. J. | *Proc. Natn. Acad. Sci. USA*, 1982, **79**, 2554–2558. |
| 2. Hopfield, J. J. | *Proc. Natn. Acad. Sci. USA*, 1984, **81**, 3088–3092. |
| 3. Amit, D. J., Gutfreund, H. and Sompolinsky, H. | *Phys. Rev. Lett.*, 1985, **55**, 1530–1533. |
| 4. Amit, D. J., Gutfreund, H. and Sompolinsky, H. | *Ann. Phys. N. Y.*, 1987, **173**, 30–67 |
| 5. Dotsenko, V. S. | *J. Phys. C*, 1987, **18**, L1017–L1021. |
| 6. Dotsenko, V. S. | *JETP Lett.*, 1986, **44**, 193–196. |

## Thesis Abstract (Ph.D.)

## **Homogenization of partial differential equations in perforated domain** by A. K. Nandakumaran

Research supervisors: Phoolan Prasad and M. Vanninathan (TIFR)
Department: Mathematics (TIFR–IISc Programme)

### 1. Introduction

Theory of homogenization in partial differential equations has a variety of applications in various branches of science[1-3]. In the present work, we study the homogenization of certain problems in a periodically perforated domain.

First we introduce the notations. Consider a bounded domain $\Omega \subset \mathbf{R}^N$, $N \geq 2$ and cover $\Omega$ with $\epsilon$-periodic ($\epsilon > 0$, a parameter) cells which are translates of $\epsilon Y$, where $Y = (-1,1)^N$. Now, from each $\epsilon$ cell remove a hole $T_{a_\epsilon}$ of size $a_\epsilon$, $0 < a_\epsilon \leq \epsilon$. Start with an open set $T \subset Y$. Then the hole in $\epsilon Y$ is $T_{a_\epsilon} = a_\epsilon T$. The perforations in other cells are simply translations of $T_{a_\epsilon} = a_\epsilon T$. Denote $\Omega_{a_\epsilon}$ or simply $\Omega_\epsilon$ the domain obtained from $\Omega$ by removing the sets $T_{a_\epsilon}$. In other words, $\Omega_{a_\epsilon}$ is a perforated domain with holes of size $a_\epsilon$ and which are arranged periodically with period $\epsilon$. Let $Y^* = Y \setminus \bar{T}$ and $S = \delta T$. In this work, we study certain boundary value problems and their dependence on the domain in which they are posed. The way the domains vary is described here.

## 2. Problem description and results

Consider the following problem. Look for the velocity $v_\epsilon$ and the pressure $p_\epsilon$ such that

$$\begin{aligned} -\Delta V_\epsilon + \nabla p_\epsilon &= f_\epsilon \text{ in } \Omega_\epsilon \\ \operatorname{div} v_\epsilon &= 0 \text{ in } \Omega_\epsilon \\ v_\epsilon &= 0 \text{ on the outer boundary} \\ v_\epsilon &= g^\epsilon \text{ on the boundary of the holes} \end{aligned} \qquad (1)$$

where $f_\epsilon$ is the source term such that $\epsilon^2 f_\epsilon \to f$ in $L^2(\Omega)$ and $g^\epsilon(x) = g\left(\frac{X}{\epsilon}\right)$, with $g$ defined on $Y$ and then to all of $\mathbf{R}^N$, periodically. $g$ has to satisfy the compatibility condition $\int_{\delta T} g.v_y = 0$, where $v_y$ is the unit normal at $\delta T$.

The aim is to study the behaviour of $V_\epsilon$ and $p_\epsilon$ as $\epsilon \to 0$. Here we assume $a_\epsilon = 0(\epsilon)$. First define the following system:

$$\begin{aligned} & -\Delta_y v_0 + \nabla_y p_1 + \nabla_x p_0 = f \text{ in } \Omega \times Y^* \\ & v_0,\ p_1 \text{ are } Y-\text{periodic},\ v_0 = g \text{ on } S,\ a.e.\ \times \in \Omega \\ & \operatorname{div}_y v_0 = 0 \text{ in } \Omega \times Y^*,\ \operatorname{div}_x \int_{y^*} v_0(x,y)\,dy = 0 \text{ in } \Omega \\ & v_x \cdot \int_{y^*} v_0\,dy = -v_x \cdot \int_S (g.v_y)y\,ds \text{ on } \Gamma = \delta\Omega. \end{aligned} \qquad (2)$$

Here $v_x$ is the unit normal at $\Gamma$.

*Theorem A:* There exist extensions $\tilde{v}_\epsilon$, $\tilde{p}_\epsilon$ of $v_\epsilon$, $p_\epsilon$ respectively to all of $\Omega$ such that $\tilde{v}_\epsilon \to v$ in $L^2(\Omega)$ weak, $\epsilon^2 \tilde{p}_\epsilon \to p_0$ in $L^2(\Omega)/\mathbf{R}$ strong and the weak limit $v$ is given by

$$v(x) = \int_{y^*} v_0(x,y)\,dy + \int_S (g.v_y)y\,dS$$

where $v_0$ and $p_0$ are given by the unique solution of (2).

*Theorem B:* Let $v$ and $p_0$ be as in Theorem A. Then, $v$ and $p_0$ satisfies the following Darcy's law:

$$\begin{aligned} \operatorname{div} v &= 0 \text{ in } \Omega \\ v &= K(f - \nabla p_0) + c \text{ in } \Omega \\ v.v_x &= 0 \text{ on } \Gamma. \end{aligned}$$

Here $K$ is a symmetric, positive definite matrix, given by certain functions which are defined in the basic cell $Y^*$. The constant vector $c$ can be represented in terms of the boundary values of $g$ and the test functions on $S$.

We also study the homogenization of spectral problems associated with Stokes, Laplacian, biLaplacian and elasticity equations. Here we briefly describe the Stokes and elasticity eigenvalue problems.

Consider the Stokes eigenvalue problem:

$$\begin{aligned} -\Delta u_\epsilon + \nabla p_\epsilon &= \lambda_\epsilon u_\epsilon \text{ in } \Omega_{a_\epsilon} \\ \operatorname{div} u_\epsilon &= 0 \text{ in } \Omega_{a_\epsilon} \\ u_\epsilon &= 0 \text{ on } \delta\Omega_{a_\epsilon}. \end{aligned} \tag{3}$$

The aim is to study the behaviour of $u_\epsilon$, $p_\epsilon$ and $\lambda_\epsilon$ as $\epsilon \to 0$ when the size of the hole $a_\epsilon$ ισ μθψη σμαλλερ τηαν τηε περιοδ $\epsilon$. In fact, we assume that

$$a_\epsilon = \begin{cases} C_0\epsilon^\alpha, \ \alpha \geq \dfrac{N}{N-2'} N \geq 3 \\ \operatorname{Exp}\left(\dfrac{-C_0}{\epsilon^\alpha}\right), \ \alpha \geq 2, \ N = 2, \ C_0 \text{ a constant.} \end{cases}$$

We have the following homogenized system:

$$\begin{aligned} -\Delta u + Mu + \nabla p &= \lambda u \text{ in } \Omega \\ \operatorname{div} u &= 0 \text{ in } \Omega \\ u &= 0 \text{ on } \delta\Omega \end{aligned} \tag{5}$$

where $M$ is a positive definite matrix obtained from some test functions introduced by Allaire[4,5].

*Theorem C (Critical case):* Let $a_\epsilon$ be as in (4) with $\alpha \dfrac{N}{N-2}$, $N \geq 3$. Let $\{u_\epsilon^l, p_\epsilon^l, \lambda_\epsilon^\lambda$ be the entire spectrum of the problem (3). Then there exist extensions $\tilde{u}_\epsilon^l$, $\tilde{p}_\epsilon^l$ such that $\tilde{u}_\epsilon^l \to u^l$ in$H_0^1(\Omega)^N$ weak, $\tilde{p}_\epsilon^l \to p^l$ in $L^2(\Omega)/\mathbf{R}$ weak, $\lambda_\epsilon^l \to \lambda^l$ *as* $\epsilon \to 0$ where $\{u^l, p^l, \lambda^l\}$ is the entire spectrum of (5).

*Theorem D (Sub-critical case):* Let $a_\epsilon$ be as in (4) with $\alpha > \dfrac{N}{N-2}$, if $N \geq 3$, $\alpha > 2$ if $N = 2$. Then one can obtain the same convergence results as in Theorem C, but the solution $\{u^l, p^l, \lambda^l\}$ satisfies the system (4) without the term Mu.

We also obtain the corrector results for $u_\epsilon$, $p_\epsilon$ and $\lambda_\epsilon$. Of course one can obtain some easy estimates on $|\lambda_\epsilon - \lambda|$. But by introducing correction $\lambda_{1\epsilon}$ to $\lambda$, we will obtain better estimate of $|\lambda_\epsilon - \lambda - \lambda_{1\epsilon}|$. We will not present the estimates here because it involves the solution of some problem in $\Omega_{a_\epsilon}$ and the test functions.

The eigenvalue problem associated with the elasticity system can be described as follows:

$$-\frac{\delta}{\delta x_j}\alpha_{ij}(u_\epsilon) = \lambda_\epsilon u_{\epsilon i} \text{ in } \Omega_{a_\epsilon}, \ i = 1, \dots N$$

$$\alpha_{ij}(u_\epsilon) = \frac{1}{2}\left(\frac{\delta u_i}{\delta x_j} + \frac{\delta u_{\epsilon j}}{\delta x_i}\right) \text{ in } \Omega_{a_\epsilon} \tag{6}$$

$$u_\epsilon = 0 \text{ on } \delta\Omega_{a_\epsilon}.$$

In this case the homogenized system is given by

$$-\frac{\delta}{\delta x_j}\alpha_{ij}(u) + (Mu)_i = \lambda\ u_i \text{ In } \Omega, \ i = 1, \dots N$$

$$\alpha_{ij}(u) = \frac{1}{2}\left(\frac{\delta u_i}{\delta x_j} + \frac{\delta u_j}{\delta x_i}\right) \text{ in } \Omega \tag{7}$$

$$u = 0 \text{ on } \delta\Omega.$$

*Theorem E (Critical case):* Let $a_\epsilon$ be as in Theorem *B* of Chapter 3. Further $\widetilde{u}^l_\epsilon \to u^l$ in $H^1_0(\Omega)^N$ weak and $\lambda^l_\epsilon \to \lambda^l$ as $\epsilon\ \lambda\ 0$. Moreover, $u^l$, $\lambda^l$ is the *i*th solution of the system (7).

In the subcritical case, the result is same as above but the homogenized system will not contain the term Mu. Moreover, the corrector results are also available.

**References**

| | |
|---|---|
| 1. Attouch, H. | Variational convergence for functions and operators, 1984, Pitman Advanced Pub. Program |
| 2. Bensoussan, A. *et al* | *Asymptotic analysis for periodic structures*, 1978, North Holland. |
| 3. Sanchez-Palencia | Non-homogeneous media and vibration theory, Lecture Notes in Physics, 127, 1980, Springer-Verlag. |
| 4. Allaire, G. | *Homogenization of Navier–Stokes equations in open sets perforated with tiny holes* (Preprint), Parts 1 and 2 |
| 5. Allaire, G. | Homogenization des equations de Navier–Stokes, These, Universite, Paris 6, 1989. |

## Thesis Abstract (Ph.D.)

**Some studies of conformal field theories on higher genus Riemann surfaces** by Narayan Behera
Research supervisors: Romesh K. Kaul and K. P. Sinha
Department: Physics

### 1. Introduction

It is of interest to develop general methods of obtaining characters and correlation functions of two-dimensional conformal field theories (CFTs) on arbitrary genus Riemann surfaces. There have been various approaches in this direction. In this work, we have developed a simple method by specific examples to provide a complete solution of CFT on an arbitrary genus surface. This method exploits the factorization properties of the characters/correlation functions on higher genus surfaces under pinching of zero- and non-zero homology cycles of the surface; and modular invariance. The holomorphic factorization of correlation functions does not occur on Riemann surfaces of genus-two or higher[1] However, one can study the ratio of correlators of a CFT with central charge c and the partition function of a single scalar field raised to the power c. This ratio is free of conformal anomaly, metric independent and modular invariant[2].

### 2. Objective

The factorization properties involved in these studies relate to the pinching limit of two types of non-trivial cycles on a Riemann surface. The cycle on the cylinder connecting two handles of a Riemann surface is called a zero-homology cycle and the cycle lying on the handle is called a non-zero homology cycle. The general idea of the factorization property under zero-homology pinching (ZHP) limit of a surface of genus $g_1 + g_2$ is that the correlation function should factorize into two correlation functions, one each on genus $g_1$ and genus $g_2$ surfaces and the propagator of the mediating primary field on the cylinder. On the other hand, under non-zero homology pinching (NZHP) limit of a genus $(g + 1)$ surface, the idea of factorization is that the correlator should factorize into a correlator on genus g surface and a propagator on the cylinder corresponding to the appropriate primary field going round the loop which is pinched. Also, the grand total of all the normalized characters/correlators (whose number is determined by fusion rules) on a given surface must be modular invariant.

By the above method, we have explicitly obtained the normalized characters and correlations for the following CFT models: (i) critical Ising model, (ii) level-one SU(2) Wess–Zumino (WZ) model, (iii) level-two SU(2) WZ model and (iv) level-one SU(3) WZ model.

### 3. Critical Ising model[3]

The critical Ising model is described by three primary fields: identity operator 1, energy operator $\epsilon$ and spin operator $\sigma$. The central charge is 1/2. We have obtained the expressions for appropriately normalized partition function $Z(\Omega)/Z_B^{1/2}(\Omega)$ and one- and two-point correlators, $<\epsilon(z)>(\Omega)/Z_B^{1/2}(\Omega)$, $<\epsilon(Z)\epsilon(W)>(\Omega)\,/\,Z_B^{1/2}(\Omega)$, and $<\sigma(z)\sigma(w)>(\Omega)/Z_B^{1/2}(\Omega)$ on genus-two surface explicitly. Also, we have presented the analysis of $Z(\Omega)/Z_B^{1/2}(\Omega)$ on arbitrary genus. Fusion rules do not allow $\sigma$-one point correlator, but $\epsilon$-point correlator on genus-one and higher surfaces are non-zero. The normalized partition functions involve all possible even $\theta$-functions, while $\epsilon$-one point correlators involve only the odd $\theta$-functions, $\epsilon$-$\epsilon$ correlators are also given in terms of even $\theta$-functions. On the other hand, $\sigma$-$\sigma$ correlators contain both even and odd $\theta$-functions. We have made use of factorization property under ZHP limit and modular invariance. We also obtain the 3-point $\epsilon$-correlators, $<\epsilon(p_2)\epsilon(Z_1)\epsilon(w_1)>(\tau)$ on torus from one-point $\epsilon$-correlator on genus-two $<\epsilon(P_2)>(\Omega)/Z_B(\Omega)$ by NZHP limits.

### 4. Some Wess–Zumino models

#### 4.1. *Level-one SU(2) Wess–Zumino model*[4]

The level-one SU(2) WZ model is described by two primary fields: an SU(2) singlet $\phi_0$ and a doublet $\phi_{1/2}$. The central charge is one. By making use of factorization under ZHP limit and modular invariance, we have written down the arbitrary genus expressions for $Z(\Omega)/Z_B(\Omega)$ and $<\phi_{1/2}(Z).\ \phi_{1/2}(w)>(\Omega)/Z_B(\Omega)$. We have also obtained expressions for 2n-point $\phi_{1/2}$–$\phi_{1/2}$ normalized correlators

$$<\left(\prod_{i=1}^{n}\phi_{1/2}(z_i).\phi_{1/2}(w)\right)>(\Omega)/Z_B(\Omega)$$

on an arbitrary genus surface by exploiting the factorization property under NZHP limit and modular invariance[5].

#### 4.2. *Level-two SU(2) Wess–Zumino model*[4]

The level-two SU(2) WZ model is characterized by three primary fields: a singlet $\phi_0$ a doublet $\phi_{1/2}$ and a triplet $\phi_1$ of SU(2). The central charge is 3/2. By exploiting factorization property under ZHP limit and modular invariance, we have obtained expressions for $Z(\Omega)/Z_B^{3/2}(\Omega)$ on genus-two and arbitrary genus-surface; and $\langle \phi_1(z).\phi_1(w)\rangle/Z_B^{3/2}(\Omega)$ and $\langle \phi_{1/2}(z).\phi_{1/2}(w)\rangle(\Omega)/Z_H^{3/2}(\Omega)$ on genus-two surface. Fusion rules forbid $\phi_{1/2}$-one point correlator. We have also surveyed the NZHP limit of genus-two characters/correlators for specific examples.

### 4.3. *Level-one SU(3) Wess–Zumino model*[6]

The level-one SU(3)WZ model is specified by three primary fields: $\phi_0$, $\phi_3$ and $\phi_{\bar{3}}$ which are, respectively, a singlet, a triplet and an anti-triplet of SU(3). The central charge is two. We have written down the correlators on genus-one surface by making use of the monodromy properties of correlators. Genus-two results are constructed next for normalized characters $Z(\Omega)/Z_B^2(\Omega)$ and two-point correlators $\langle\phi_3(z, \bar{z}).\ \phi_{\bar{3}}(w, \bar{w})\rangle(\Omega)/Z_B^2(\Omega)$ in terms of classical theta functions associated with SU(2) by making use of fusion rules, modular invariance and factorization property under ZHP limit. Then the results are generalized to an arbitrary genus surface. We have also obtained the normalized four-point correlators

$$\left\langle\left(\prod_{i=1}^{2}\phi_3(z_i).\phi_{\bar{3}}(w_i)\right)\right\rangle(\Omega)/Z_B^2(\Omega)$$

by NZHP limits of the characters with $(\phi_3)$ representation going round the two pinched blobs.

### 5. Conclusion

We have demonstrated by examples that it is enough to know all genus characters to solve a CFT. Any correlator can be obtained from an appropriate character by a suitable set of pinchings along zero-homology and non-zero homology cycles of the Riemann surface. In particular, this also would provide a simple method of obtaining any-point correlators on the sphere from higher genus characters.

### References

1. Belavin, A and Knizhnik, V. *Phys. Lett. B*, 1986, **168**, 201–206.
2. Mathur, S. D. and Sen, A. *Phys. Lett. B*, 1989, **218**, 176–184.
3. Behera, N., Malik, R. P. and Kaul, R. K. *Phys. Rev. D*, 1989, **40**, 1993–2003.
4. Malik, R. P., Behera, N. and Kaul, R. K. *Phys. Rev. D*, 1991, **43**, 1243–1255.
5. Malik, R. P., Behera, N. and Kaul, R. K. *Mod. Phys. Lett. A*, 1990, **5**, 2643–2649.
6. Kaul, R. K., Malik, R. P. and Behera, N. *Phys. Rev. D*, 1990, **41**, 478–483.

---

## Thesis Abstract (Ph.D.)

## **Non-ohmic conduction, electrical switching and magnetoresistance of quasi one-dimensional conductors at high pressures** by T. Ravindran

Research supervisor: S. V. Subramanyam
Department: Physics

### 1. Introduction

The thesis describes the experimental work on the transport properties of quasi one-dimensional charge transfer complexes down to liquid helium temperature, high pressures up to 8 GPa and high magnetic fields up to 6 Tesla. It includes non-ohmic conduction, electrical switching under pressure at a temperature of 300 K and magnetoresistance studies at different temperatures.

### 2. Experimental

To study these transport properties, a flow-type cryostat, microprocessor-based temperature controller and Bridgman anvil high-pressure clamp cell were designed and constructed. For dc and pulsed I–V measurements, a low (15 V) and a high voltage (250 V) constant current source, and pulse generator were designed and constructed. Pulses were generated by a microcomputer. Switching time was recorded in a storage oscilloscope. Magnetoresistance measurement was done up to a field of 6 Tesla in Janis cryostat. Samples of methyltriphenylarsonium–$(TCNQ)_2$, benzidine–DDQ and o-toluidine–DDQ were studied.

### 3. Results and discussion

Electrical switching observed in the three charge-transfer complexes mtpa–$(TCNQ)_2^1$, benzidine–DDQ[2] and o-tolidine–DDQ[3] has common origin and the basic features observed in these three complexes are the same. Current–voltage characteristics are analysed on the basis of variation of mobility with field, Schottky emission, Poole–Frenkel effect or by space-charge limited current. Non-ohmic conduction in these samples can be explained either by Poole–Frenkel effect or by space-charge limited current. Pulsed I–V measurement shows the heating contribution to non-ohmicity. At high fields of the order of $3 \times 10^5$ V/m samples switch from low-conducting OFF state to high-conducting ON state with $\sigma_{ON}/\sigma_{OFF} \sim 10^3$. Switching time recorded for the sample mtpa–$(TCNQ)_2$ is 0.5 ms which shows that switching is a slow process. If the switching is caused by pure electronic process the switching time will be of the order of nanoseconds or at least microseconds as observed in chalcogenide glasses and other systems. After switching, differential negative resistance region associated with noise is observed in the I–V measurement. Powder diffraction pattern of mtpa–$(TCNQ)_2$ in the normal and the switched state shows a structural change. Temperature dependence of resistivity of switched sample of mtpa–$(TCNQ)_2$ down to liquid helium temperature shows that the plot of $\ln \sigma$ *vs* $1/T^{1/4}$ is a straight line typical to that of amorphous materials. Magnetoresistance of the ON state of mtpa-$(TCNQ)_2$ at different temperatures shows that relative change of resistance $\delta R_H/R_0$ is proportional to $H^2$ up to a field of 6 Tesla. Electrical switching observed in these three complexes is explained as due to field-induced thermal switching which leads to a structural change.

### References

1. Ravindran, T. and Subramanyam, S. V. Nonlinear electric transport and switching phenomenon in methyltriphenyl arsonium–$(TCNq)_2$ under pressure, *Synth. Metals*, 1992, **46**, 317–324.
2. Ravindran, T. and Subramanyam, S. V. Electrical switching in benzidine–DDQ under pressure, *Bull. Mater. Sci.*, 1991, **14**, 1205–1211.
3. Ravindran, T. and Subramanyam, S. V. Electrical switching and memory phenomena in o-toluidine–DDQ under pressure, *Pramana*, 1991, **37**, 147–151.

---

## Thesis Abstract (Ph.D.)

## **The contribution of polarons, bipolarons and dipolar relaxations to charge transport in conducting polymers** by M. Reghu

Research supervisor: S. V. Subramanyam
Department: Physics

### 1. Introduction

The present work is principally concerned with the transport properties of conducting polymers down to 1.3 K, while varying parameters like the magnetic field, pressure and frequency. In intrinsically quasi-one-dimensional materials, conductivity and anisotropy in conductivity are due to the delocalised $\pi$-electrons along the polymer chain. Apart from the applications envisaged, the interest in these materials is to study the new physics associated with novel excitations present in conducting polymers. The ground state excitations in conducting polymers are solitons, polarons and bipolarons, unlike the electrons and holes in inorganic semiconductors. Even though the evidence for nonlinear excitations, like polarons and bipolarons, in nondegenarate polyconjugated systems like polypyrrole and polythiophene are known from optical and spin measurements, their participation in charge transport is not yet clearly understood. The motivation of the present work is to study the role of these carriers in low-temperature conductivity and magnetotransport. Besides, theoretical interpretation has been offered for the temperature dependence of conductivity in various temperature regimes and the low-frequency energy absorption in these systems[1].

### 2. Experimental

Samples of polypyrrole and polythiophene at various concentrations of polarons and bipolarons were prepared by electrochemical doping. In polypyrrole, polarons are stable excitations at low doping concentrations, while polarons combine together to form bipolarons at high doping levels. Thus, polypyrrole is an ideal system to study their different contribution to charge transport. At low temperatures the conductivity of a highly doped sample is two orders of magnitude smaller than that of the less doped one, due to the presence of greater number of bipolarons in the former sample. This is due to the high activation energy required for bipolaron hopping while compared to that of polaron hopping. Bipolaron hopping through the intermediate dissociated polaron states may lead to a crossover in conductivity between lightly and highly doped samples. This may be observable at very low temperatures, when the thermal energy is not sufficient for such virtual process. The above mechanism of bipolaron hopping results in variation of the effective number of charge carriers, which is reflected in the conductivity measurements.

### 3. Low-temperature conductivity measurements

The conduction in doped polyconjugated systems involves ionization of carriers from deep-trapped states, having $T^{-1/2}$ dependence, hopping from localised states, having $T^{-1/4}$ dependence, and tunneling at very low temperatures, having a $T^{-1}$ dependence. The observed $T^{-1/3}$ fit in doped samples is due to the interplay between $T^{-1/2}$ and $T^{-1/4}$, which is in agreement with the theoretical model. Even though this exponential temperature dependence of conductivity is similar to that of Mott expression, the microscopic mechanism of conductors in doped polyconjugated systems is more complicated than the simple variable range hopping model. Even at extremely low doping levels conductivity increases by many orders of magnitude without a corresponding increase in the number and mobility of charge carrier. This could be explained by the three-dimensional interactions between the polymer segments due to the low dielectric constant and large polarizability of $\pi$-electron systems.

The temperature dependence of conductivity of doped polypyrrole is very much weaker when compared to that of doped polythiopene. This is due to the difference in the energetics of polaron and bipolaron formation in polypyrrole and polythiophene. The strong temperature of conductivity in polythiophene is due to the smaller number of polarons and the enhanced stability of bipolarons in polythiophene.

The deviation from the hopping fit at temperatures below 4·2 K is due to the possibility of tunnel transport in disordered polaronic systems[2,3]. The transition from hopping to a tunneling-dominated process can be observed either by increase in conductivity or by saturation of conductivity. This transition is suppressed by magnetic field on account of the shrinkage of the Bohr radius of localised states. This observation gives an insight into the tunneling mechanism, which is due to the inter-site tunnel percolation in disordered polaronic systems.

### 4. Magnetoresistance

The large positive magnetoresistance observed in doped polypyrrole at very low temperatures is in agreement with the above tunneling process. From magnetoresistance measurements, transport property parameters like the effective mobility and density of states at various concentrations of polarons and bipolarons were calculated[4,5]. Low-frequency ac measurements provide information about the low-energy relaxation processes usually observed in polymer chains due to the polarization of side groups, dipoles, etc. These measurements could offer us a better understanding of the relationship between the chemical structure, disorder and the electronic properties of polyconjugated systems.

### References

| | |
|---|---|
| 1. Reghu, M , Vaidyanathan, R. S. Prasad, V. and Subramanyam, S. V. | Miniature high pressure cell for transport property measurements down to 2K, *Rev Sci. Instrum.*, 1990, **61**, 1336–1338 |
| 2. Reghu, M. and Subramanyam, S. V. | Tunnel transport process in doped polypyrrole, *Solid St. Commun.*, 1990, **72**, 325–329 |
| 3. Reghu, M and Subramanyam, S. V. | Suppression of tunnel transport by magnetic field in polypyrrole, *Phys. Lett. A*, 1990, **145**, 371–375. |
| 4. Reghu, M., Subramanyam, S. V. and Chatterjee, S. | Contribution of polarons and bipolarons to low temperature conductivity in doped polypyrrole, *Phys. Rev. B*, 1991, **43**, 4236–4242. |
| 5. Reghu, M., Subramanyam, S. V. and Chatterjee, S. | Pressure induced incommensurate to commensurate transition in $K_3Cu_8S_6$, *Solid St. Commun.*, 1989, **69**, 949–952. |

## Thesis Abstract (Ph.D.)

### **Subcritical deflagration and prognostication of combustion from microscopic features of fuel and catalyst in ammonium perchlorate systems: A thermodynamic approach** by K. Sridhara

Research supervisor: K. Kishore

Department: Inorganic and Physical Chemistry

### 1. Introduction

Composite solid propellants (CSP) are a major source of chemical energy for space vehicles and missiles. Prediction of CSP performance from ingredient characteristics is a long-cherished goal for propellant chemists. The present study brings out the importance of the understanding of condensed-phase combustion processes in CSP, ammonium perchlorate (AP) decomposition, deflagration and their modeling. Compared to AP, amazingly, the role of polymeric hydrocarbon fuel-binders, such as carboxy-terminated polybutadiene (CTPB)/hydroxy-terminated polybutadiene (HTPB), has received less attention[1]. The importance of binder characteristics in CSP combustion and modeling studies is projected in this work. Apart from usual burn-rate modifiers in CSP[2], the advantages and multifunctional role of currently used ferrocene derivatives have been highlighted.

AP monopropellant burns only above a critical pressure (20 atm) known as the low-pressure deflagration limit (LPL)[3]. The emphasis of the present investigation is on the understanding of AP deflagration in the subcritical regime, below LPL, labelled as regime I′. AP can be made to burn by boosting the initial temperature ($T_0$) or by adding a fuel. To get an insight into the dependence of burning rate ($\dot{r}$) on the microscopic behaviour of the fuel, AP + model fuels consisting of aliphatic dicarboxylic acids of molecular weight 118 to 202 have been selected to simulate CTPB and obtain better understanding of the complex binder combustion. The dependence of the structural parameters such as molecular weight, functionality and *cis–trans* isomerism have been studied. Prognosticative capability of the catalyst to predict $\dot{r}$ from structural features, hitherto unknown, is identified.

### 2. Results and discussion

Considering the perfect differential equation where $\dot{r}$ is a function of pressure and $T_0$, a novel thermodynamic model[4] has been devised to understand AP deflagration in regime I′. This model identifies the true activation energy of pure condensed-phase reactions occurring just below the surface, gas-phase activation energy of the reactions occurring just above the surface and reveals the mechanism operative. The observed low value for the true condensed-phase surface activation energy for AP in regime I′ corresponds to $HClO_4$-catalyzed decomposition of AP, corroborated by: (i) pH measurement of the quenched surface, (ii) the decomposition of AP recrystallized from the acid medium, (iii) the micrographs of a cluster of dents formed on the quenched surface, (iv) the reported[5] activation energy for the electrical conductance of AP combustion which matches with the observed value. Further, the decrease of temperature sensitivity of burning rate ($\sigma_p$) with pressure in AP deflagration[6] has been verified by this model. Hess's cycle[7], articulated for AP to go from $T_0$ to the products in the flame through its various physicochemical pathways, identifies the critical enthalpic conditions for sustenance of AP deflagration at LPL, below and above LPL and has been verified from temperature profile analysis. Similar analysis done for powder AP combustion indicates that 16% of AP particles enter the free board region and undergoes combustion very near to the surface.

Extension of the thermodynamic model to AP + aliphatic dicarboxylic acid and AP/CTPB propellant systems suggests that, in the case of former, the rate-controlling step in the condensed phase is similar to that in pure AP, while, in the case of the latter, it is the softening of CTPB. This model also explains 'intermittent burning', 'plateau burning' and 'flameless combustion' in CSPs based on polybutadiene acrylic acid, polyurethane and polysulfide binders, respectively.

The critical enthalpy of the condensed phase necessary to augment the surface heat release in regime I′ so that the LPL could be reduced to 1 atm and $T_0$ of 27°C is realised in the combustion of AP + succinic acid instead of AP + malonic acid mixture which does not burn as predicted. In fact, AP + malonic acid burns above $T_o$ of 440°C since the combustion of malonic acid occurs essentially as acetic acid which is the product of its decomposition.

A new parameter called molecular weight sensitivity of burning rate ($\sigma_m$) has been defined. A plot of ln $\dot{r}$ as a function of molecular weight reveals three slopes. Acids in slope I form anhydrides, whereas those in slope II do not. However, the volatilization temperature of the acids in slope II coincides with that of AP phase transition, and the more reactive cubic AP, due to its interaction with the fuel, suppresses the volatilization rate. In slope III, CTPB fragments to an average fragment size equal to sebacic acid. As the molecular weight of the acid increases, the extent of condensed phase reactions ($\Delta H_1$, measured from the temperature profile analysis), temperature gradient in a thin zone beneath the burning surface, average surface heating rate and surface temperature increases and thereby governs $\dot{r}$, whereas the distance of the occurrence of exothermic condensed phase reaction from the surface reduces. A heating rate of 470°C/s observed for the AP + sebacic acid compares closely with those encountered in CSP[8]. This systematic trend in the variation of different physicochemical factors as a function of molecular weight suggests that $\sigma_m$ has an important significance in the combustion scene of CSP and, being corrigible with $\sigma_p$, is useful in modeling studies. Sebacic acid, derivatized to different end groups and $\dot{r}$ studied as composite with AP, reveals a good correlation with the Taft constant suggesting that $\dot{r}$ decreases as the end groups become more electron withdrawing. Combustion of AP + maleic acid and AP + fumaric acid shows that $\dot{r}$ of the *trans* isomer is about 6% higher than the *cis* isomer.

A unique approach of group contribution has been adopted to predict the $\dot{r}$ of propellants containing ferrocene-based catalysts, which compares well with the experimental value. Although specific to a particular class of the catalyst, such studies would be beneficial in designing novel catalyst systems possessing anticipated performance.

## References

1. Kishore, K. *AIAA J.*, 1979, **17**, 1216–1217.
2. Kishore, K. and Sunitha, M. R. *AIAA J.*, 1979, **17**, 1118–1125.
3. Boggs, T. L. and Kraeutle, K. J. *Combust. Sci. Technol.*, 1969, **1**, 75–93.
4. Kishore, K. and Sridhara, K. *Proc. R. Soc. Lond. A*, 1993, **440**, 55–76.

5. Melik, G. G V. and Marshakov, V N — *Fiz Goreniya i Vzryva*, 1987, **23**, 15–20
6. Kishore, K and Sridhara, K. — *J. Propulsion Power*, 1986, **2**, 193–194.
7. Kishore, K and Gayathri, V. — Chemistry of ignition and combustion of ammonium perchlorate-based propellants. In *Fundamentals of solid propellant combustion*, *Prog. Astr. Aeronaut.*, Vol. 94, pp. 53–119, 1984, AIAA
8. Price, E W. — *J. Spacecraft Rockets*, 1983, **20**, 320.

---

## Thesis Abstract (Ph.D.)

## **Theoretical studies of the α-cleavage and hydrogen abstraction reactions of some ketones and thiones** by K. Sumathi

Research supervisor: A. K. Chandra
Department: Inorganic and Physical Chemistry

### 1. Introduction

Carbonyl and the thiocarbonyl compounds undergo a variety of photochemical reactions[1,2]. Norrish type I cleavage reaction (α-cleavage reaction) and intermolecular hydrogen abstraction reactions have been considered in the present study.

### 2. Results and discussion

When an unsaturated system is excited, it leads to the cleavage of a σ-bond situated in position α to the chromophore. In the case of a carbonyl compound, the primary step is the cleavage of α-bond to produce a radical pair comprising an alkyl and an acyl radical.

A brief account of the α-cleavage reactions of ketones and thioketones is given[1–3]. Correlation diagrams that have been used to understand the α-cleavage processes are discussed. They often fail to reveal the small energy barriers in the potential energy surfaces. Reliable data on the activation energies of most photochemical unimolecular reactions are scarce. A scrutiny of the values of the activation parameters for the α-cleavage processes reported in the literature shows large discrepancies for the same molecule and unexpectedly large contrasts between different molecules. Intermolecular hydrogen abstraction reactions of ketones and thioketones have also been discussed. Perturbation procedure employed to understand this reaction is briefly outlined.

*Ab-initio* studies of the radical decomposition of some carbonyl and thiocarbonyl compounds are described and the results of the calculations already reported on some ketones and thioketones are compiled[4,5]. In the present work, calculations are done on acetaldehyde and formaldehyde using the Gaussian-70 program with STO-3G and 4-31G basis sets. It is observed that the *ab-initio* calculations using the small basis set Gaussian functions, overestimate the activation barriers for the photofragmentation reactions. If these values are to be believed then none of these molecules can undergo photodissociation from their lowest triplet or the first excited singlet states. Reliable and more accurate values can be obtained only if large basis set *ab-initio* calculations with extensive configuration interaction (C.I.) and geometry optimisation at the C.I. level and at the points on the potential energy surface are performed. However, such calculations are highly labour-intensive and costly even for simple organic molecules. Thus, our next step has been to apply suitably modified semi-empirical methods, which need relatively less computer time, to these processes in a series of ketones and thioketones to predict a reliable trend in the heights of the activation barriers.

An account is given of the semi-empirical molecular orbital studies of the radical decomposition of some symmetric and non-symmetric ketones in their lowest excited states[6]. The CNDO/2-CI (complete neglect of differential overlap) and the MINDO/3-CI (modified intermediate neglect of differential overlap) methods are used to calculate the potential energy surfaces (PES) of the reactions in a few ketones. Self-consistent field (SCF) procedures used in the semi-empirical theories are described. A brief discussion is given on the use of CI in the SCF procedures and the method of calculation of the PES. Calculated activation barriers for the photodissociation into radicals in the lowest[1,3] $(n,\pi^*)$ surfaces obtained by the CNDO/2-CI procedure are approximately an order of magnitude higher than that obtained by the MINDO/3-CI procedure. However, both these methods lead to approximately similar trends. In an α-cleavage process, when an α-bond is elongated along its bond direction, perpendicular motion of the carbonyl carbon with respect to planar geometry of the reactant is found to be an important component of the reaction coordinate[7]. In a non-symmetrical ketone, the selectivity of cleavage of the α-bond is related to the amount of the bonding and antibonding characters in the highest occupied and the lowest unoccupied σ-m.o.s, respectively, of the ketone.

Theoretical PES for the α-cleavage processes in some thiocompounds including thioformaldehyde are studied[8]. The semi-empirical procedures outlined earlier are followed. Although the activation barrier for the α-cleavage processes in thioformaldehyde is within the upper limit required for a unimolecular reaction to compete with phosphorescence, the non-observation of photocleavage is probably due to the effective quenching of the triplet state by the ground state. It is seen that, in the case of cyclopropenethiones, the .cleavage process can take place in its lowest triplet state with an activation barrier of about 52 kJ/mole. In β-dithiolactones, a similar process can take place in its lowest excited singlet state as its activation barrier is still lower.

The standard perturbation procedure is employed within the framework of a semi-empirical method (MINDO/3) to understand the process of intermolecular hydrogen abstraction reaction of a ketone and a thioketone from a hydrocarbon[9]. The reaction coordinate involves the motion of the two molecules and the stretching of the donor C–H bond towards the atom to which the hydrogen atom is transferred. While neither the activation barriers nor the geometries of the transition states can be predicted accurately from this analysis, the different photochemical reactivities of a ketone and a thione towards a common hydrogen donor can be understood satisfactorily. This is possible by a qualitative study of the relative positions of the energy levels of the lone pair m.o. of the ketone or thione $H_2CX$ ($X = 0,S$) and the highest occupied molecular orbital (HOMO) of the hydrogen donor for the reaction in the $(n,\pi^*)$ state. If the reaction is from the $(\pi,\pi^*)$ state, the energy levels of the highest occupied π-m·o. of $H_2CX$ and the HOMO of the hydrogen donor become important. Results show that hydrogen abstraction by the heteroatom is observed in ketones and thiones in their $(n, \pi^*)$ state by an in-plane process. The thiocarbonyl carbon atom in thiones in their $(\pi, \pi^*)$ state can, however, abstract a hydrogen atom in a plane perpendicular to the molecular plane.

**References**

| | |
|---|---|
| 1. Coyle, J. D. and Carless, H. A. J. | *Chem. Soc. Rev.*, 1972, **1**, 465–480. |
| 2. Dalton, J. C. and Turro, N. J. | *A. Rev. Phys. Chem.*, 1970, **21**, 499–560. |
| 3. Ramamurthy, V. | In *Organic photochemistry*, Vol. 7, (Padwa, A., ed.), 1985, Marcel Dekker. |
| 4. Paul de Mayo | *Acc. Chem. Res.*, 1976, **9**, 52–59 |
| 5. Scaiano, J. C. | *J. Photochem.*, 1973, **2**, 81–118. |
| 6. Lewis, D. F. V. | *Chem. Rev.*, 1986, **86**, 1111–1123 |
| 7. Sumathi, K. and Chandra, A. K. | *J. Photochem. Photobiol. A*, 1987, **40**, 265–277. |
| 8. Sumathi, K. and Chandra, A. K. | *J. Org. Chem.*, 1988, **53**, 1239–1243. |
| 9. Sumathi, K. and Chandra, A. K. | *J. Photochem. Photobiol. A*, 1988, **43**, 313–327. |

## Thesis Abstract (Ph.D.)

## **Radical cyclisation routes to terpenes and furans** by G. Sundarababu
Research supervisor: A. Srikrishna
Department: Organic Chemistry

### 1. Introduction

Free radicals are reactive intermediates of considerable importance in the development of organic

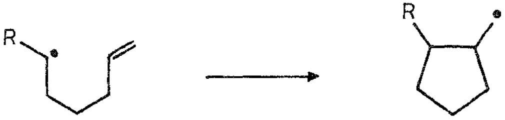

EQUATION 1.

chemistry. In addition to important functional group transformations, the formation of carbon–carbo bonds by addition or cyclisation reactions is often possible under mild and selective conditions[1,2]. Variou aspects of radical cyclisation reactions (eqn 1) and their application in natural products synthesis, *e.g.* cuparenoids, and furans is reported in this work.

### 2. Synthesis of cuparenoids

Total syntheses of (±)–laurenes (**2**) and (**3**) and formal total syntheses of (±) – cuparenones (**4**) and (**5** along with two unsuccessful approaches to cuparene (**1**) based on radical cyclisation reactions wer achieved[3-5] (Chart I).

Two approaches to cuparene (**1**), *via* the cyclisation of radicals **6** (Scheme 1) and **7** (Scheme 2), wer attempted. The radical precursor bromoolefin **8** was prepared starting from the readily availabl isobutyrophenone **9** *via* the ketone **10**, tertiary alcohol **11** diol **12** and enemesylate **13**. Radical cyclisatio ($^n$Bu$_3$SnH, AIBN, $C_6H_6$, 0·02M) of the bromide **8** furnished the 6-*endo-trig*-cyclised product **14** exclusively. Analogously, the other radical precursor, hexenyl bromide **15** was synthesised starting from propiophenone **16** *via* the esters **17** and **18**, tertiary alcohol **19**, diol **20** and enemesylate **21**. Radical cyclisation of the bromide **15** also furnished exclusively, the 6-*endo-trig*-cyclised product **22**.

Total synthesis of laurenes (**2**) and (**3**) (Scheme 3) was achieved *via* the cyclisation of ε-acetylenic acetal **24** *via* the aldehyde **25**, eneacetal **26** and aldehyde **27**. The acetal **24** was transformed to the xanthate **28**, the radical precursor, *via* the aldehyde **29** and the alcohol **30**. Radical cyclisation of the vinyl radical **31**, generated from the enyne **32**, obtained from the aldehyde **29**, provided the 6-*endo*-cyclised product **33** only.

Synthesis of the enome **34**, a precursor[6] to β-cuparenone (**5**) was developed *via* the cyclisation of the radical **35** (Scheme 4). The radical precursor, bromoacetate **36**, was synthesised starting from the aldehyde **25** *via* the enyne **37**. Radical cyclisation of the bromo acetate **36** furnished a 1:3:1.5 mixture of the

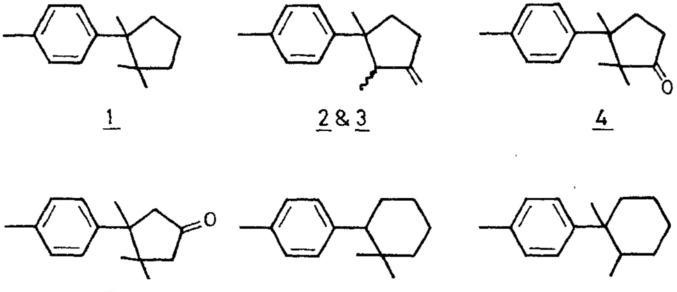

1

2 & 3

4

5

14

22

CHART I.

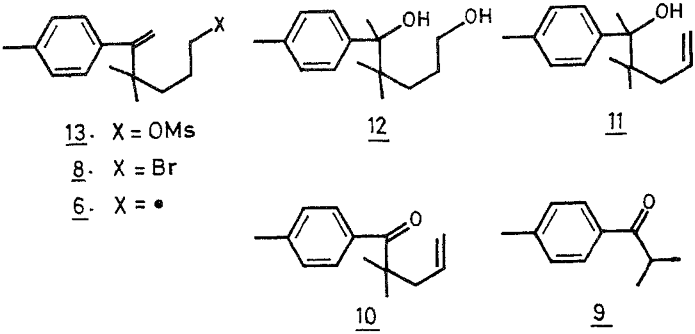

SCHEME 1

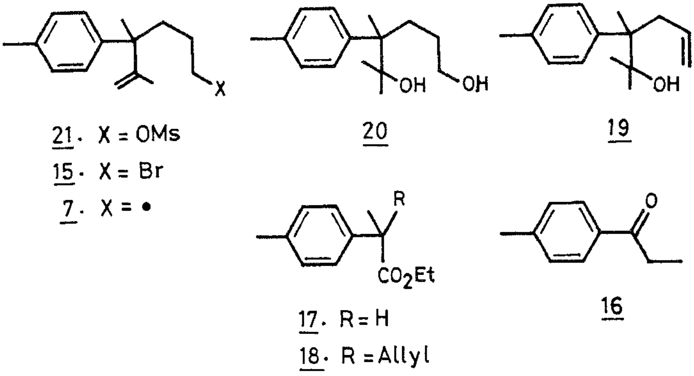

SCHEME 2.

stannylated product **38**, the 5-*exo-dig*-cyclised product **39** and the rearranged acetate **40**. The major product, cyclised acetate **39**, was converted into the enone **34** *via* the alcohol **41**.

A short route to α-cuparenone (**4**) *via* a combination of Claisen rearrangement and a radical cyclisation reaction was developed (Scheme 5). Mercuric acetate catalysed, one pot Claisen rearrangement of the cinnamyl alcohol **42**, obtained from 4-methyl acetophenone, furnished the pentenal **43**, which was homologated to the hexenal **44** *via* a Wittig reaction. Cyclisation of the radical anion **45**, derived from the hexenal **44**, followed by oxidation of the resultant alcohol furnished a 1:6 mixture of the cyclopentanone **46**, a precursor[7] to α-cuparenone (**4**).

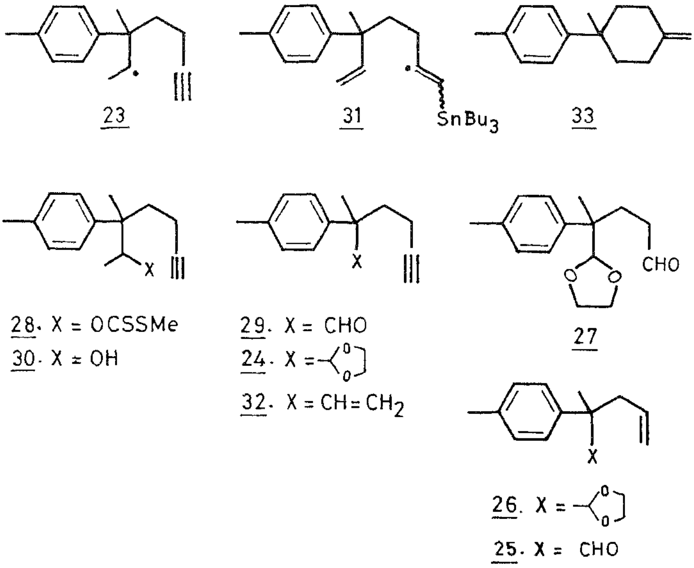

SCHEME 3.

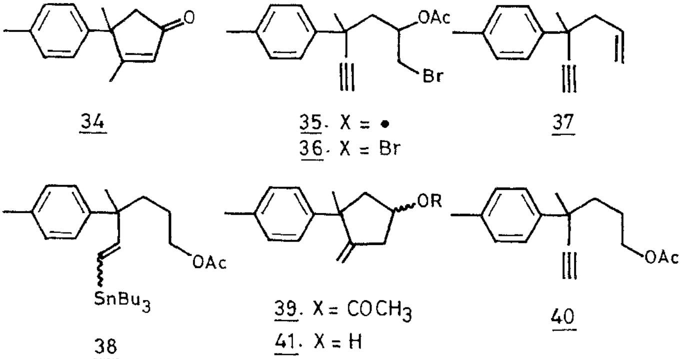

SCHEME 4.

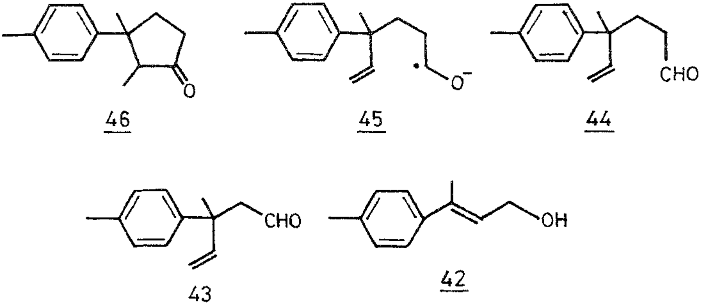

Scheme 5.

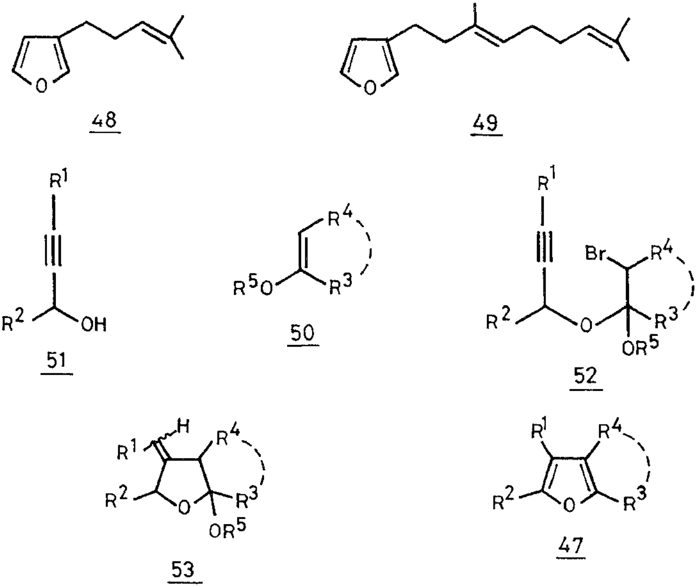

Scheme 6.

### 3. Synthesis of furans

Synthesis of various substituted furans **47**, *e.g* , 3-mono, 2,3-di, 2,3,5-tri and 2,3,4,5-tetrasubstituted[8], including the two naturally occurring furanoterpenes, perillene (**48**) and dendrolasin (**49**), based on radical cyclisation reaction has been achieved (Scheme 6). N-Bromosuccinimide (NBS) bromination of vinylethers **50** in the presence of propargyl alcohols **51** furnished radical precursors, bromoacetals **52**. The 5-*exo-dig* cyclisation of the radical derived from the bromoacetal **52** using *in-situ*-generated catalytic $^{n}Bu_3SnH$ ($^{n}Bu_3SnCl$, $NaBH_3CN$, $^{t}BuOH$) in the presence of a catalytic amount of AIBN, generated the 3-alkylidenetetrahydrofurnans **53**. Acid-catalysed aromatisation of the cyclised products **53** furnished the furans **47**.

### References

1. RAMAIAH, M — *Tetrahedron*, 1987, **42**, 3541–3676.
2. CURRAN, D. P. — *Synthesis*, 1988, 417–439 and 489–513.
3. SRIKRISHNA, A AND SUNDARABABU, G — *Tetrahedron Lett* , 1989, **30**, 3561–3562
4. SRIKRISHNA, A. AND SUNDARABABU, G — *Tetrahedron*, 1990, **46**, 3601–3606.
5. SRIKRISHNA, A. AND SUNDARABABU, G. — *Tetrahedron*, 1991, **47**, 481–496.
6. GREENE, A E., LANSARD, J-P , LUCHE, J-L. AND PETRIER, C. J — *J. Org. Chem.*, 1984, **49**, 931–932.
7. EILBRACHT, P., BLASS, E. AND ACKER, M. — *Chem. Ber.*, 1985, **118**, 825–839.
8. SRIKRISHNA, A. AND SUNDARABABU, G. — *Tetrahedron*, 1990, **46**, 7901–7910.

## Thesis Abstract (M.Sc. (Engng))

## **The role of galvanic interactions in the bioleaching of mixed sulphides** by N. Jyothi

Research supervisor: K. A. Natarajan
Department: Metallurgy

### 1. Introduction

Production of commercially acceptable individual concentrates through flotation from multimetal sulphides has been a difficult task due to complex mineralogy, finer mineral dissemination and differences in the grindability of associated sulphides. A combination process involving initial bulk flotation followed by selective dissolution of the desired mineral could prove to be commercially attractive in the processing of such difficult to beneficiate ores. In this respect, selective bioleaching of complex sulphides is more advantageous than other conventional hydrometallurgical processes[1]. Selectivity in mineral dissolution could be achieved through electrochemical means: making use of either the role of galvanic interactions or the influence of an applied potential on oxidative or non-oxidative mineral dissolution[2]. Such a selective mineral dissolution brought out either due to the galvanic potential difference or the influence of an applied potential could be significantly enhanced in the presence of autotrophic bacteria such as *Thiobacillus ferrooxidans*.

### 2. Experimental programme

Pure mineral samples of pyrite (Py), chalcopyrite (Cp), galena (Gal) and sphalerite (Sp) were used in all the studies. In addition to these, some leaching tests were also carried out using a typical lead–zinc–copper ore (from Ambamata, Gujarat).

Rest potentials of the various sulphide minerals in a bacterial leaching medium were measured both in the presence and absence of *T. ferrooxidans*. Besides, the combination potential and galvanic current existing in different binary, ternary and quaternary combinations were also measured.

Both shake flask and column-leaching experiments were carried out to understand the effect of the ratio as well as the type of mixing of the various minerals on bioleaching.

Scanning electron microscopic (SEM) observations were made to understand the surface morphology of leached surfaces and to reveal bacterial attachment, if any.

The effect of an applied potential on sphalerite and chalcopyrite dissolution from a bioleaching medium was also investigated. The potential at which selective dissolution of sphalerite with negligible chalcopyrite dissolution could be achieved was also established. The effect of the applied potential on the growth of *T. ferrooxidans* was monitored through estimation of the protein content in the system. Various mechanisms involved in the electrochemical bioleaching of sphalerite are discussed with respect to sphalerite dissolution, bacterial activity and ferric–ferrous redox reactions.

### 3. Main results and conclusions

The sulphide minerals mentioned above could be arranged in the form of a galvanic series with respect to their relative electrochemical activities. The following order depicts the arrangement of the minerals as a galvanic series.

| | |
|---|---|
| Sphalerite | Active |
| Galena | ↑ |
| Chalcopyrite | ↓ |
| Pyrite | Noble |

The effect of mixing other minerals with sphalerite (the most active mineral) in different ratios and combinations on the dissolution of sphalerite was studied. Sphalerite, mixed with either pyrite or chalcopyrite, was found to undergo faster dissolution. Again, by mixing larger amounts of the nobler mineral (either pyrite or chalcopyrite) with a small amount of sphalerite, zinc dissolution was found to be significantly enhanced.

External addition of pyrite to a complex lead–zinc–copper sulphide ore enhanced zinc dissolution very significantly.

In shake flask leaching studies, a continuous mineral–mineral contact could not be established because the mineral particles make and break contact with each other during agitation. Thus, it becomes difficult to monitor any galvanic effect on a continuous basis. To overcome this problem, minerals were arranged as a static bed one over the other, packed in different layers, in an air lift percolator and the lixiviant percolated through the static mixed bed. Ternary combinations involving pyrite, chalcopyrite and sphalerite were arranged in the following order: (a) Sp–Py–Cp; (b) Sp–Cp–Py; (c) Cp–Sp–Py. Both copper and zinc dissolution from the above mineral mixtures were monitored. Zinc and copper extraction from the arrangements (a) and (b) were found to be similar but higher than that from the arrangement (c). The type and nature of the mineral–mineral contact thus influence the mineral dissolution.

To bring out clearly the manifestation of galvanic effect in a binary sulphide mineral couple, the leaching behaviour of a chalcopyrite–pyrite mixture in the presence and absence of an intermediate insulating layer of quartz was also studied. The copper extraction from chalcopyrite which was in direct immediate contact with pyrite was found to be significantly higher than that from the chalcopyrite sample kept separated from the pyrite layer through a layer of quartz. For efficient dissolution of an active mineral from a mixed sulphide system, intimate mineral–mineral contacts are thus highly essential.

Potentials at which maximum dissolution of chalcopyrite and sphalerite would occur were established. Results depicted in Fig. 1 illustrate that at an applied potential of $-500$ mV only sphalerite undergoes selective dissolution from a mixture of sphalerite and chalcopyrite. Detailed electrochemical bioleaching

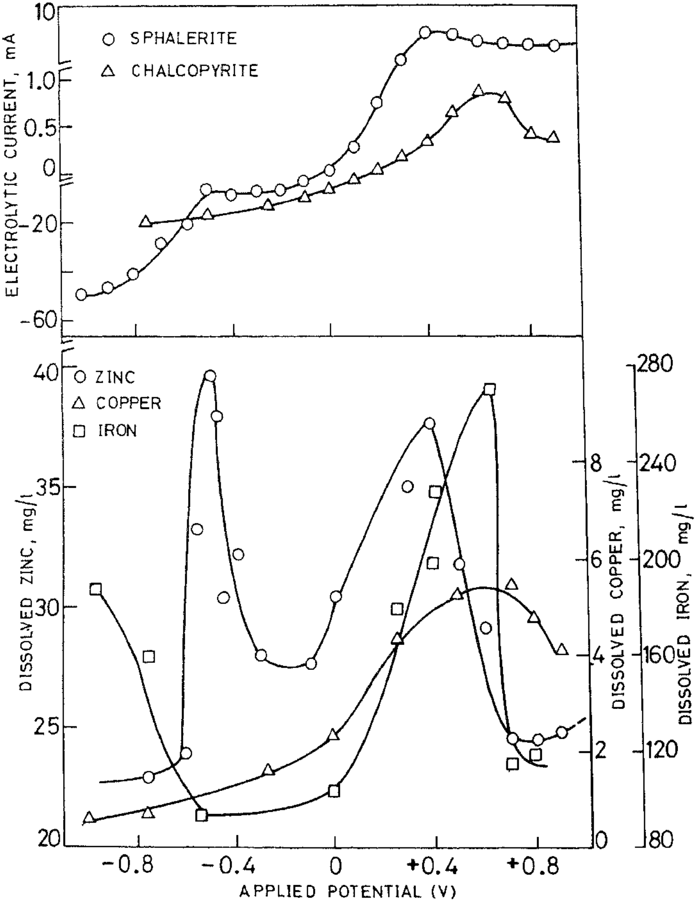

FIG. 1. Variation of measured current and dissolved metal ion concentrations as a function of applied potential in the bioleaching of sphalerite and chalcopyrite.

experiments on the dissolution of sphalerite revealed that the presence of *T. ferrooxidans* in the medium accelerates selective zinc dissolution. There was also a significant increase in the biomass during bioleaching under an applied potential of −500 mV.

SEM studies of the leaching residues revealed significant corrosion of the active mineral surfaces after contacting with a nobler mineral.

**References**

| | |
|---|---|
| 1. Natarajan, K. A. and Iwasaki, I. | *Sep. Sci Technol.*, 1983, **18**, 1095–1111. |
| 2 Natarajan, K. A , Iwasaki, I and Reid, K J | In *Recent progress in biohydrometallurgy* (G. Rossi and A E. Torma, eds), 1983, pp. 169–184, Associazone Mineraria Sarda, Italy. |

---

## Thesis Abstract (Ph.D.)

**Study of some three-dimensional effects in bolted joints** by N. Sundarraj
Research supervisors: T. S. Ramamurthy and B. Dattaguru
Department: Aerospace Engineering

### 1. Introduction

Joints are essential to connect parts of structural components, and to interconnect sub-assemblies of large-scale structural systems. Various types of structural joints are being used in technological practice: bolted joints are the most commonly used among these, wherever periodic assembly and disassembly are needed and whenever articulation is to be provided for. These joints are sources of high-stress concentration and are often potential locations of failure. Accurate analysis of these joints is of considerable significance for structural design purposes.

The problem of load transfer in a double shear lap joint is dealt with in this work. The joint consists of three flat plates with a central plate to the two outer plates. The joint could be of an interference, neat or clearance fit, depending on the bolt diameter being larger, equal to or smaller than that of the hole. The bolt is tightened by application of torque on the nut to provide clamp-up pressure between the plates. A complete understanding of the stress and deformation pattern in such a joint requires a three-dimensional analysis. The major problem in developing analysis of these joints is the requirement of multi-body contact stress analysis. Progressive application of load in these problems would lead to changes of contact/separation areas resulting in a nonlinear moving boundary value problem. The complexity of the structure requires finite element approach for the stress analysis and this needs be coupled to an interactive routine to determine the changing contact/separation boundaries.

Various aspects in the load transfer in bolted joints were studied earlier by simplified approaches[1]. Considering each plate in a state of two-dimensional plane stress, load transfer through bearing was studied including partial contact behaviour. Such analysis does not consider the plate clamping by bolt and ignores the thicknesswise variation of stress distribution. The effects of bolt clamp-up pressure alone were studied by some earlier workers in an axisymmetric joint between circular plates and this work is related to flange joints where there is no inplane load transfer between the plates[2,3]. In these studies, the modelling of self-equilibrating clamp-up load had certain assumptions. Wherever the bolt could be considered rigid, it was modelled as uniform indentation on the plates and the cases of long elastic bolts were modelled as uniform stress on the bolt at the centre section. Such models are not acceptable in short elastic bolts as those in shear joints considered in the present work.

### 2. Special techniques for analysis

To study the double shear lap joints including the effects of bolt clamp-up pressure the following two

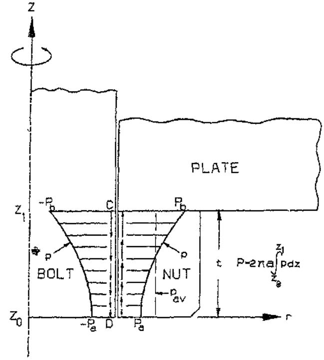

FIG. 1. Clamp-up load model.

special developments are carried out regarding the use of frontal solver in the finite element software and on modelling the bolt clamp-up load transfer.

### 2.1. *Dummy element with modified frontal solver*

The iterative method of analysis for contact stress problems in bolted joints could be expensive, unless some special features are introduced into the technique. For this purpose, computationally efficient software using frontal solver is developed along with appropriate pre- and post-processors. The frontal solver is used to eliminate all the degrees of freedom except those needed for contact stress analysis. A dummy element is introduced into the element library whose connectivity is identified with the degrees of freedom where the conditions could be either contact or separation and where external load is applied on the joint. This element has zero stiffness so that the total stiffness is not altered and only the reduced stiffness is conveniently generated with respect to those degrees of freedom. The iterative process is carried out on smaller order matrices and the appropriate boundary conditions including multi-point constraints in the contact region are imposed during the process. The pre- and post-processors have special modules for automatic mesh generation, mesh viewer, through-thickness stress chart, polar chart, stress surface chart, X–Y charts, and colour-shaded stress contours. The mesh generator has special features to automatically identify the degrees of freedom of dummy element (for contact stress analysis) for three-dimensional problems based on the experience of simpler axisymmetric analysis.

### 2.2. *Clamp-up pressure model*

Torque tightening results in load transfer along the interface between the bolt shank and the nut interface. Based on experimental results available in literature and the physics of the problem, load transfer across this interface is idealised as a parabolic pressure distribution (Fig. 1). The constants of the parabolic distribution are determined such that they ensure the bolt to be in tension and the nut to be in a compression due to clamp-up load. This model is validated by (i) a sensitivity analysis, and (ii) by comparing the results using this model with earlier experimental results. The sensitivity analysis showed that any deviation in the assumed distribution at the bolt–nut interface affects only the results in the close vicinity of this interface and the overall load transfer mechanism in the joint and the stress and deformation pattern away from this interface are not affected. This bolt clamp-up pressure model is used to carry out parametric study on axisymmetric joints between two or three plates and some of the results are compared with earlier analytical and experimental results[4].

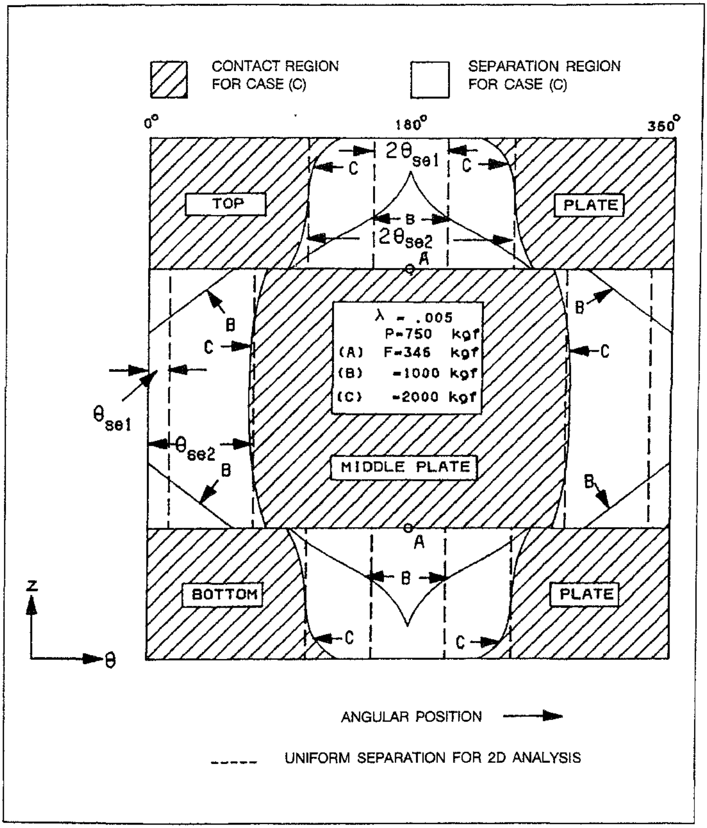

FIG. 2. Extent of separation region with plate load at plate hole.

### 3. Three-dimensional effects

Using the software tools developed and the clamp-up pressure model, three-dimensional effects in double shear lap joint are studied in two stages. In the first stage, the joint is considered with an interference fit bolt where there is full contact along the bolt–hole interface to start with. The inplane loads on the joint are restricted to the range which do not cause bolt hole interfacial separation. For this case, an axisymmet-

**Table I**
**Comparison of load for onset of separation ($\lambda = \cdot 005$)**

| | *Pin joint (2-D)* | *Finger tight joint* | *Clamped joint ($P = 750$)* |
|---|---|---|---|
| Separation load $f_{cr}$ | 2749 | 1368 | 822 |
| Gradient $\delta\sigma_\theta/\delta F$ | 0·1497 | 0·3194 | 0·1825 |

ric part of the joint, with the outer circular boundary being nearly 20 times the diameter of the hole, is analysed under non-symmetric loading. On each individual plate of the joint, the stress boundary conditions on this notional outer boundary are determined from the well-known Kelvin's solution for point load in an infinite plate. When the outer boundary is considered to be large, it is assumed that the details of bolt–hole interface do not influence the stresses on it. Harmonic analysis of such a configuration provided significant information on thicknesswise variation of stresses, the bending of the elastic bolt, the loads for onset of separation and certain solutions in pre-separation zone to compare with full three-dimensional solutions. Numerical studies showed that the clamp-up load and the elasticity of the bolt play a significant role in the load transfer in the joint. The clamp-up load causes bending of the plates and an early (with respect to load) initiation of separation. Similarly, the bolt flexure result in early initiation of separation so that separation initiates at loads much smaller for an elastic bolt compared to a rigid bolt. The gradient of maximum hoop stress which is an important parameter for the fatigue behaviour of the joint, however, improves with bolt clamp-up pressure (Table I). The choice of bolt clamp-up load for a given inplane load transfer in the joint can be evaluated from this type of analysis.

In the second stage, a three-dimensional finite element analysis of double shear lap joint is carried out. Eight-node isoparametric brick elements are used to model the joint and the benefits of computational economy with the software tools developed are utilised to a maximum extent. A comparison of these results with those obtained earlier showed that axisymmetric analysis under non-symmetric loading predicted the maximum stresses in the joint within 17% of the three-dimensional analysis, but the distributions differ to an extent of 30% at certain locations. The post-separation behaviour of the joint is analysed by three-dimensional analysis and the results are presented on the growth of separation (Fig. 2) and stress variations. Stresses in the elastic bolt are evaluated for a particular configuration for which experimental results are available in literature and the comparison is excellent.

## 4. Conclusion

The study of three-dimensional effects shows that the clamp-up pressure and the bolt flexibility have a clear influence on the load transfer in bolted joints. The clamp-up pressure produces beneficial effect of reducing the maximum stress gradient. Both clamp-up pressure and bolt flexure work together and produce detrimental effects of reducing the load for separation and increasing the stress concentration. Computational limitations have restricted the study of the effects of finite friction. Apart from it, joints between composite plates, analysis of multiple fastener joints and analysis in thermal environments are identified as areas for further research in relation to this problem.

## References

| | |
|---|---|
| 1. Ghosh, S. P. | *Analysis of joints with elastic pins*, Ph.D. Thesis, Department of Aerospace Engng, Indian Institute of Science, Bangalore, 1978. |
| 2. Thompson, J. C., Sze, Y., Strewel, D. G. and Jofriet, J. C. | The interface boundary conditions for bolted flanged connections, *Trans. ASME, J. Pressure Vessel Technol.*, 1976, **98**, 277–282. |
| 3. Gould, H. H. and Mikic, B. B. | Areas of contact and pressure distribution in bolted joints, *Trans. ASME, J. Engng Ind.*, 1972, **94**, 864–870. |
| 4. Sundarraj, N., Dattaguru, B., Krishnamurthy, T. and Ramamurthy, T. S. | Analysis of flange joints with elastic bolt, *Nucl. Engng Des*, 1987, **100**, 41–48. |

Thesis Abstract (Ph.D.)

## **A general procedure for evaluation of crack closure integral in problems of fracture mechanics** by K. Badari Narayana

Research supervisors: B. Dattaguru, T. S. Ramamurthy and K. Vijayakumar
Department: Aerospace Engineering

### 1. Introduction

Fracture mechanics is concerned with the analysis of the influence of an existing flaw on the strength and the life of a structural component. Analyses based on linear elastic fracture mechanics (LEFM) are adequate in most practical situations which involve only small scale yielding around crack tips. For effective utilization of these analyses, accurate estimation of fracture parameters such as stress intensity factors (SIF) or strain energy release rates (SERR) G, in cracked bodies is required. Finite element method (FEM) is a very effective and powerful tool for the analysis of structures. From FEM solutions, these parameters are extracted using (a) displacement or stress/force methods for SIF, (b) virtual crack extension, (c) J-integral, and (d) modified crack closure integral (MCCI) for G.

The present work deals with the use of FEM to fracture mechanics and its applications to practical problems. In-depth understanding of fracture behaviour, particularly, in mixed-mode situations is needed in the design of complex structures for high-technology applications. MCCI method has an excellent potential for the analysis of such problem. A systematic development of MCCI technique is the main subject of investigation in this work.

### 2. Development of MCCI

Crack closure integral (CCI) is based on the concept proposed by Irwin[1] that SERR during virtual crack extension is equal to the energy required to close the crack back to the original size. The SERR can conveniently be estimated for a 2D crack configuration (Fig. 1a) using CCI from the analysis of two configurations with crack lengths differing by $\Delta a$. On the other hand, it is possible to estimate SERR from a single analysis as long as $\Delta a$ is very small and this procedure is known as modified crack closure integral (MCCI). Using the concept of MCCI, and introducing polar coordinate system with origin at the crack tip, the expression for mode-I SERR $G_I$ can be written as

$$G_I = \underset{\Delta a \to 0}{Lt} \, (1/2\Delta a) \int_0^{\Delta a} \sigma_y \, (r = x,\ \Theta = 0) \; U_y \, (r = \Delta a - x,\ \Theta = \pi) \; dr \qquad (1)$$

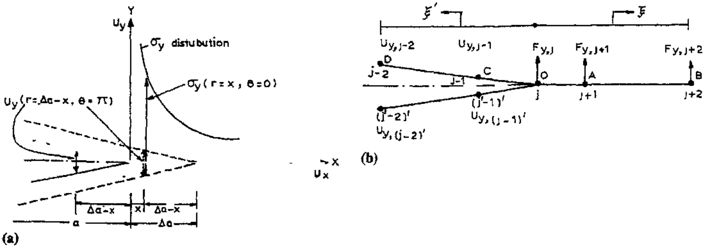

FIG. 1.(a) Original and extended crack configurations, and (b) crack opening displacements and nodal forces.

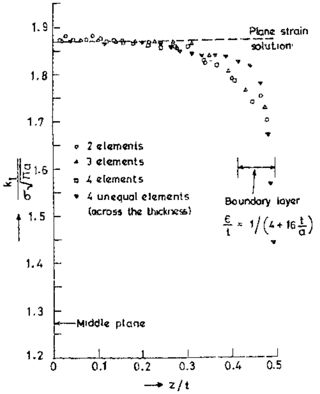

FIG. 2. Variation of SIF along the crack front from four equal sub-area integration: CCT specimen (h/w=0·5, a/w =0·5 and t/a=0·5).

where $\sigma_y$ ($r = x$, $\Theta = 0$) is the stress distribution ahead of the crack tip; $U_y$ ($r = a-x$, $\Theta = \Pi$) is the relative opening displacement between the crack faces and $a$ is virtual crack increment.

The MCCI method is initiated by Rybicki and Kanninen[2] for 2D crack problems modelled with CTS and 4-noded elements. MCCI expressions are further modified for 6-noded triangular elements by Buchholz[3]. In the present work, a general procedure is presented for deriving the element-dependent MCCI expressions for both 2- and 3-dimensional crack problems.

### 3. MCCI procedure for 2 and 3D crack problems

First, a general procedure for estimating SERR is proposed for 2D problems. This was demonstrated for 4-noded and both 8-noded regular and singular elements. Typical expressions for mode-I SERR, $G_I$ using 8-noded singular elements are as follows:

$$G_I = (1/2\ at)\ [(C_{11}F_{y,\,j} + C_{12}F_{y,\,j+1} + C_{13}F_{y,\,j+2})\ (U_{y,\,j-1} - U_{y,\,(j-1)}),$$
$$+ (C_{21}F_{y,\,j} + C_{22}F_{y,\,j+1} + C_{23}F_{y,\,j+2})\ (U_{y,\,j-2} - U_{y,\,(j-2)})] \quad (2)$$

where $F_{y,\,j}$, $F_{y,\,j+1}$, . . . and $U_{y,\,j-1}$, $U_{y,(j-1)}$ . . . are the nodal forces and displacements (Fig. 1b) and

$$C_{11} = 33\Pi/2 - 52 \qquad C_{12} = 17 - 21\Pi/4 \qquad C_{13} = 21\Pi/2 - 32$$
$$C_{21} = 14 - 33\Pi/8 \qquad C_{22} = 21\Pi 16\text{-}7/2 \qquad C_{23} = 8 - 21\Pi/8.$$

One can derive similar MCCI expressions for mode-II SERR, $G_{II}$.

The general procedure proposed is also adopted to 3D crack problems to obtain appropriate SERR expressions. The 3D structure is modelled with 8-noded brick elements and the crack closure integral is estimated over an area in the plane of virtual crack extension. These MCCI expressions provide the distribution of average value of $G$ for each element along the crack front. To obtain accurate $G$-distribu-

**Table I**

**Comparison of present SIF solution for CI specimen using 12-noded elements ($w/t = 2{\cdot}0$; $a/w = 0{\cdot}5$; $\nu = 0{\cdot}3$)**

SIF correction factor $F = K_I t \sqrt{w/P}$; $\beta = F/F_{\text{plane strain}}$

| *Type of element* | *SIF estimation method* | *Total DOF used* | $\beta$ |
|---|---|---|---|
| 6-noded singular[5] | COD approach | 1980 | 0·99 |
| 6-noded singular[6] | Force method | 1875 | 0·99 |
| 20-noded singular | COD approach | 1497 | 1·07 |
| Present 3D elements | MCCI | 1410 | 0·99 |

tions along the crack front, it is necessary to estimate $G$ at a number of points along the crack front. This is achieved by an effective post-processing technique called the 'sub-area integration', which has been evolved and used in the present work. The technique is validated for several through and part-through crack problems. Figure 2 shows the variation of SIF along the crack front for a CCI specimen, showing the boundary layer effect obtained by using this technique.

### 4. Development of special crack tip elements and application to practical problems

Special crack tip elements[4] such as 5-noded triangular and 6-noded quadrilateral elements for 2D problems and 12-noded brick elements for 3D problems are developed to achieve an economical solution by using these elements at the crack tip/front. Table I gives a typical example showing the economy of solution obtained by using the 12-node brick element along the crack front.

Application of the special crack-tip elements developed along with the general MCCI procedure has been demonstrated for the analysis of a pin-loaded lug with diametrically opposite cracks originating from the hole boundary. The present software is used to predict the fatigue life estimations and these are compared with the available experimental results[7].

### 5. Conclusions

With the procedures and techniques developed in this work application of MCCI procedure is expected to become much wider, in particular, to mixed-mode crack problems and to achieve an economical and accurate solution for many practical problems treated with in the realm of linear elastic fracture mechanics (LEFM).

### References

1. Irwin, G. R. — *Handb. Phys.* Vol. 6, pp. 551–590, 1958.
2. Rybicki, E. F. and Kanninen, M. F. — *Engng Fracture Mech.*, 1977, **9**, 931–938
3. Buchholz, F. G. — *Proc. 4th World Congr. Exhib. in FEM*, Interlaken, 1984, pp. 650–659.
4. Badari Narayana, K., Dattaguru, B. Ramamurthy, T. S. and Vijayakumar, K. — *Engng Fracture Mech.*, 1990, **36**, 945–955.
5. Tracey, D. M. — *Nucl. Engng Des.*, 1974, **26**, 282–290.
6. Raju, I. S. and Newman, J. C. Jr — *NASA-TN-D-8414*, 1977.
7. Schijve, J. and Hoeymakers, A. H. W. — *Engng Mater. Struct.*, 1979, **1**, 185–201.

Thesis Abstract (M.Sc. (Engng))

## A study on acoustic emission characterisation of fatigue damage in unidirectional glass fiber composites by M. Ramachandra Bhat

Research supervisor: C. R. L. Murthy
Department: Aerospace Engineering

### 1. Introduction

Fatigue failure in composite materials is a result of accumulation and interaction of different types of failure modes such as matrix cracking interface debonding and fiber breakage. Fatigue damage progression in these materials occurs in stages[1]. Different failure modes contribute to the cumulative damage to different extent with specific modes dominating in individual stages. So, to understand fatigue damage progression in composites, we need to identify and characterise the individual failure modes as also estimate the cumulative damage at different stages and the contribution of different failure modes Thus, one needs a tool which can be used online to identify the failure modes and to monitor their progress with respect to increase in fatigue cycles. Acoustic emission technique is the most suitable candidate for this purpose.

### 2. Contribution of the thesis

The work presented was taken up with the primary intention of understanding fatigue damage in composites. Keeping in mind that fatigue damage is progressive in nature and is governed by accumulation and interaction of different failure modes taking over dominance in stages, acoustic emission technique with its basic principles and unique features has been proposed as the most suitable candidate with the help of experimental investigations. A survey of published literature has shown that though some investigators have studied the application of AE technique for evaluation of composites [2-4], a consistent and consorted approach does not seem to have been adopted to understand damage initiation and growth under fatigue loading in composites using acoustic emission. Thus, in this work emphasis is placed on experimental investigations to understand the process in terms of initiation and progression of fatigue damage as it occurs using AE. And, unidirectional glass fiber-reinforced epoxy composite material has been chosen in view of its simplicity and suitability for studying fatigue damage. Acoustic emission data were collected and analysed from a set of 30 specimens.

The first result of the data analysis using cumulative events shows that using acoustic emission technique, three distinct stages of damage progression can be identified which are correlated to a short first stage with matrix cracking as the dominant failure mode, a long second phase as interface debonding and a short final stage as fiber breakage. Further, to estimate the contribution of each of the failure modes in each stage, pattern classification was attempted through cluster analysis. This analysis yielded three natural groups in the data set which are directly correlated to the three failure mechanisms. By estimating the number of events belonging to each group at any stage in the fatigue life, a quantitative assessment of cumulative damage at a given instant and hence residual life prediction can be made.

### 3. Conclusions

Acoustic emission technique is the most suitable candidate for studying fatigue damage in composite materials. Using the technique three distinct stages of damage progression could be identified which are related to different failure mechanisms. The failure mechanisms could be characterised through multiparameter analysis using pattern recognition method. It has been shown that it is feasible to predict residual life through quantitative estimation of damage at a given stage using acoustic emission.

### References

1 Talreja, R. *Fatigue of composite materials*, 1987, pp. 19–21, Technomic Publishing Co.

2 Williams, J. H Jr and Lee, H. S. Acoustic emission monitoring of fiber composite materials and structures, *J. Composite Mater*, 1978, **12**, 348–370.

| | |
|---|---|
| 3 Sato, N, Kurauchi, T and Kamigonto, O | Detection of damage in composite materials by thermo-acousto emission measurement, *J Composite Mater*, 1988, **22**, 447–458. |
| 4 Hamstad, M A | Acoustic emission, a tool for composite material studies. *Expl Mech*, 1986, **26**, 7–15 |

# Thesis Abstract (Ph.D.)

## **Investigations of cuprate superconductors and other complex oxide systems by electron microscopy and cognate technique** by G. N. Subbanna

Research supervisor: C. N. R. Rao
Department: Materials Research Centre

### 1. Introduction

Trasmission electron microscope is the ideal instrument to investigate a range of inhomogeneities and defect structures in solids While X-ray and neutron diffraction provides the determination of unit cells of periodic structures, electron diffraction in the electron microscope provides further information about the superstructure formation. Selected area diffraction (SAED) convergent beam electron diffraction (CBED) and micro-diffraction add to the various ways of carrying out electron diffraction experiments in the electron microscope. The high-resolution electron microscope image (HREM) obtained by allowing more than two beams to interfere reveal local structural variations involving polymorphic, polytypic and polytypoid reactions. In this work, extensive electron microscopic studies have been carried out on high-temperature cuprate superconductors and other complex oxides.

### 2. Experimental

Polycrystalline powders of cuprates and other complex oxide systems reported in this work were prepared by the ceramic route. Metal–ceramic composites were prepared by the sol–gel route JEOL JEM 200CX and Philips EM 301 electron microscopes were used for TEM and HREM studies Samples for the microscopic examination were prepared by fine-grinding the powders in a suitable medium (acetone, ethyl alcohol, etc.) using a mortar and pestle. The resultant slurry was then deposited on holey carbon grids. Through focus images were recorded in the magnification range 2 to $5 \times 10x^5$.

### 3. Results and discussion

#### 3.1. *High-temperature superconducting cuprates*

The discovery of high $T_c$ superconductivity in the La–Ba–Cu–O system by Bednorz and Muller[1] has created a great excitement in materials science. The identification of the phase responsible for superconductivity in the Y–Ba–Cu–O system, namely, $YBa_2Cu_3O_7$, was independently carried out in this Institute as early as March 1987[2] Oxygen stoichiometry plays an important role in the superconducting transition temperature of this cuprate. $YBa_2Cu_3O_{7-\delta}$ $(0{\cdot}0 < \delta < 0{\cdot}6)$ with $T_c$s in the range of 45–93K shows twins in the electron microscope bright-field images (Fig. 1). Twins result from the tetragonal-orthorhombic transformation. It has been established that twins have no direct influence on the superconducting transition temperature of these cuprates. The 60K superconducting phase $(\delta = 0{\cdot}3\text{–}0{\cdot}4)$ is metastable and transforms to the more stable orthorhombic and tetragonal phases on annealing. Electron microscopy of 124 cuprates $(LnBa_2Cu_4O_8)$ and 247 cuprates $(Ln_2Ba_4Cu_7O_{15})$ where Ln = rare earth or Y prepared by the ceramic route in a flowing oxygen atmosphere show intergrowths of each other or with the 123 cuprate. The 123 cuprates prepared with excess CuO often show fringes of 124 in a matrix of 123. Both 124 and 247 cuprates yield 123 and CuO on heating above 1100K.

Superconducting bismuth cuprates of the type $Bi_2(Ca, Sr)_{n+1}Cu_nO_{2n+4}$ and $Bi_2Sr_2Ca_{1-x}Ln_xCu_2O_8$ have incommensurate modulated structure. It has been shown that this modulated structure has little to do with the superconducting properties of these cuprates.

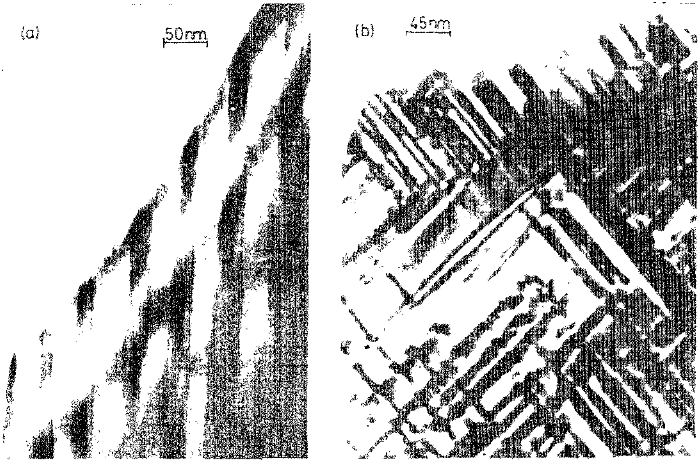

FIG 1 (a) Bright-field image of twins in $YBa_2Cu_3O_7$, (b) 90° twins in $YBa_2Cu_3O_7$

Electron microscopy of superconducting thallium cuprates of the formula $Tl_2Ba_2Ca_{n-1}Cu_nO_{2n+4}$ and $TlBa_2Ca_{n-1}Cu_nO_{2n+3}$ show random intergrowth of different members. Besides intergrowths, other types of defects have also been identified in the various superconducting cuprates.

### 3.2. *Aurivillius oxides*

Layered bismuth oxides of the general formula $Bi_2A_{n-1}B_nO_{3n+3}$ ($n = 1$ to 6), first described by Aurivillius[3], have been investigated by high-resolution electron microscopy (HREM) In these oxides, the A cation is generally $Bi^{3+}$, $Ba^{2+}$, etc While the B cation is $W^{6+}$, $Ti^{4+}$, $Nb^{5+}$, $Fe^{3+}$, etc., and $n$ refers to the number of Perovskite layers[3]. The Perovskite layers of the composition $(A_{n-1}B_nO_{3n+1})^{2-}$ occur between the $(Bi_2O_2)^{2+}$ layers. A highly ordered structure is observed up to $n =$ member, whereas higher members show dislocations and stacking faults arising from the side-stepping of $(Bi_2O_2)^{2+}$ layers and ferroelectric domains. We also observe unusual superstructures The Aurivillius family of oxides also form recurrent intergrowth structures consisting of alternate sequences of $n$ and $n+1$ perovskite layers interleaved by $(Bi_2O_2)^{2+}$ layers. Crystal structures and dielectric properties of three recurrent intergrowth structures formed by the $n = 3$ and the $n = 4$ members, namely, $Bi_9Ti_6CrO_{27}$, $Bi_9Ti_6FeO_{27}$ and $BaBi_8Ti_7O_{27}$ have been investigated. Just as the parent oxides, the intergrowth oxides also exhibit ferroelectricity and accordingly belong to the non-centrosymmetric space group Cmm2. The ferroelectric Curie temperatures of the intergrowths are in the range of 630–1070K.

### 3.3. *Bismuth vanadates*

Structure and properties of $Bi_2VO_{5.5}$ ($Bi_4V_2O_{11}$), the vanadium analogue of the $n = 1$ member of the Aurivillius oxides, have been characterized[4]. $Bi_4V_2O_{11}$ is semiconducting and ferroelectric with a Curie temperature 720K Electron diffraction studies indicate superstructure in the ab-plane. Lattice images show domains. We have also examined the structure and properties of a vanadate of the composition $Bi_{1.33}V_2O_6$ ($Bi_2V_3O_9$). At ambient temperature, this oxide is not ferroelectric and the electrical properties are similar to those of $Bi_4V_2O_{11}$. High-resolution images of $Bi_{1.33}V_2O_6$ showed the oxide to be layered and the possibility of random intergrowths.

### 3.4. *Metal–ceramic composites*

The sol–gel method has been employed to prepare a series of metal–ceramic composites[5]. Metal particles (Pt, Ni) in $Pt–Al_2O_3$ and $Ni–Al_2O_3$ composites prepared by the reduction of the xerogels have been investigated by electron microscopy and X-ray diffraction. The average size of the metal particles increases with the metal content in these composites. Pt atoms exhibit a greater tendency to form metal clusters than the Ni atoms. At low metal concentrations (~0·25wt%), the number of atoms in the metal particles is in the range 100–400. Studies on $Ni–ZrO_2$ composites show that $ZrO_2$ matrix is fairly crystalline even in the xerogel, the crystallinity decreasing with increasing Ni content. The crystalline phase is partly or fully cubic and transforms to the monoclinic phase on heating to higher temperatures. The cubic–monoclinic phase transition of $ZrO_2$ has been investigated in the xerogels with the incorporation of cations such as $Mg^{2+}$, $Ca^{2+}$, and $Cu^{2+}$, in addition to $Ni^{2+}$; the transformation has also been studied in metal–$ZrO_2$ composites (metal = Ni and Cu). The cubic form in the pure $ZrO_2$ xerogel transforms to the monoclinic form in the 570–820K temperature range. It increases to 870–1220K for xerogels with cations $Ca^2$, etc., and in composites. The kinetics of the transformation follows the exponential rate law. The activation energy of the transformation in pure xerogel is rather small ($30 kJmol^{-1}$). The activation energy of the transformation is significantly higher in the xerogels incorporating different cations ($E_a$ = $220–330 kJmol^{-1}$) compared to the composites ($E_a$ = $65–145 kJmol^{-1}$)[6].

**References**

| | |
|---|---|
| 1. Bednorz, J. G. and Muller, K. A. | *Z. Phys. B*, 1986, **64**, 189–193. |
| 2. Rao, C. N. R. *et al* | *Nature*, 1987, **326**, 856–857. |
| 3. Aurivillius, B | *Ark. Kemi*, 1950, **2**, 519–524. |
| 4. Varma, K B. R , Subbanna, G N.<br>Guru Row, T. N. and<br>Rao, C. N. R. | *J. Mater. Res.*, 1990, **5**, 1–5 |
| 5. Subbanna, G. N and Rao, C. N. R | *Mater. Res. Bull.*, 1986, **21**, 1465–1471 |
| 6. Subbanna, G. N. and Rao, C. N. R. | *Eur J. Solid St. Inorg. Chem.*, 1989, **26**, 7–11. |

---

## Thesis Abstract (M.Sc. (Engng))

### **Design and implementation of a VLSI floating point arithmetic processor** by G. N. Rathna

Research supervisor: K. Parthasarathy
Department: Electrical Engineering

### 1. Introduction

There has been an ever-increasing need for high-speed and high-precision numeric computational devices in image processing, computer graphics, robotics, model simulation, CAD/CAM, measurement and other applications[1]. Floating point computation is most suitable for these applications, because it keeps the precision of operation high in spite of the wide dynamic range. The improvement in the numeric performance of sequential and parallel machines is also achieved today largely through 'attached' high-speed floating point accelerators. Traditionally, floating point arithmetic has been slow in software and expensive in hardware. The availability of basic design and simulation tools has stimulated the VLSI implementation of such floating point processors in a manner that will permit a number of them to be used so as to operate on real vectors of a reasonable size.

### 2. Review of architectures and technology for floating point arithmetic

The present work is concerned with alternative architectures, design techniques, the simulation and fabrication technologies for the implementation of a floating point processor unit (FPU). The heart of any FPU performing floating point multiplication and addition is the fraction multiply and add circuitry. Hence, the design of the architecture for this unit plays a very important role in the overall design of the FPU.

The important architectures are:

i) Serial or sequential multipliers
ii) Fast serial parallel multiplier
iii) Parallel or array multipliers.

Sequential multipliers use simpler hardware but the speed achieved through these multipliers is relatively low, while higher speeds can be achieved with array multipliers at the expense of higher hardware complexity and power consumption[2]. Where there is hardware restriction and better speeds are required, the fast serial parallel multiplier offers a very favourable tradeoff in that it uses lesser hardware than parallel multipliers, but is faster than its sequential counterpart

Two approaches of design for the FPU in VLSI technology have been closely investigated. They are: i) Gate array technology, and ii) Full custom or standard cell technology.

### 3. ASIC implementation and conclusion

As a case study, the complete indigenous design of a 16-bit floating point multiplication and addition is developed in the gate array technology[3]. A gate array is a matrix of transistors and the processing cost is less, because these transistors are prefabricated and only the required connections for the circuitry have to be established at the fabrication level. The disadvantage is that some of the transistors are not used, causing chip area to be wasted, resulting in increased cost.

The simulation results obtained from the standard cell technology are two and a half times faster than that of gate array technology. This is mainly due to better technology and improved design used in the standard cell technology. Due to this, the 32-bit floating point multiplication (conforming to IEEE 754 standard) speed for a single FPU is expected to be 2–3 megaflops. Detailed simulation results for the devices prove the technological feasibility of the design for fabrication.

Finally, an MIMD structure with several of these devices connected to each of the processing elements of the system as 'vector-coprocessor' will yield 10–15 mflops. Several numerically intensive applications that exhibit parallelism at coarse as well as fine granularities, a common feature in much of scientific computations, can benefit from such an architecture.

### References

1. Kung, S. Y. *VLSI array processors*, 1988, Prentice-Hall.
2. Gnanashekaran, R. A fast-serial parallel binary multiplier, *IEEE Trans.*, 1985, **C-34**, 741–744.
3. Rathna, G. N., Sridhar, M. K., Parthasarathy, K and Nandy, S. K. Floating point processor with gate-array technology: A preliminary design, *Inter. Workshop on VLSI Design*, 1990.

## Thesis Abstract (Ph.D.)

## **Reinforced soil technique for soft/expansive soils** by Bindumadhava

Research supervisors: B.R. Srinivasa Murthy and A. Sridharan
Department: Civil Engineering

### 1. Introduction

Economical improvement of mechanical properties of the soil is one of the aims of a geotechnical engineer.

*Reinforced soil technique is a method by which overall stability of the soil can be improved* Reinforced soil is a composite construction material composed of soil fill strengthened by inclusion of tensile elements. The increased stability is through frictional interaction between the soil and reinforcement, which results in the reinforced soil structure acting as a coherent gravity[1]. Due to its economy, ease in construction and adaptability to most of the soil structures, this technique is replacing the other conventional ground improvement methods. One of the potential fields of application where reinforced soil can prove to be effective is in the improvement of the bearing capacity of the soil. Although the concept of reinforcing the weak foundation soil is not new, it is yet to be examined to solve the problems connected with expansive soils, *viz.*, to improve stability of foundations upon inundation, control of heave, etc. Further, soft soils are not generally used as backfill material in reinforced soil structures. One of the main reasons for this is the low frictional characteristics of these soils[2]. The main goal of this investigation has been to examine the possibility of extending reinforced soil technique to solve the problems of soft and expansive soils.

## 2. Evaluation of interfacial friction

Suppression of lateral deformation of soil, through frictional interaction between soil and reinforcement, under externally applied load is the primary mechanism of reinforced earth. Understanding the mechanism of mobilization of interfacial friction is essential before extending the reinforced earth technique to solve the problems of soft and expansive soils. A detailed examination of the mechanisms of mobilization of interfacial friction has been made. Three mechanisms, *viz.*, sliding, bonding and bearing have been identified[3] and from these explanations have been offered for the variation in the values of coefficient of interfacial friction obtained from different testing methods. Depending on the reinforcement characteristics like extensibility, rigidity and hardness, surface roughness and striations, planar and grid etc., the type reinforcements have been grouped. The range of values of angle of interfacial friction has been specified with respect to the angle of internal friction of the soil, for different testing methods. With the help of experimental results obtained from different types of sliding tests and pull-out tests, the influence of surface characteristics, extensibility and rigidity of reinforcement on the mobilization of interfacial friction has been examined. Further, boundary effects on test results have been discussed in detail. A method has been identified to quantify the boundary effects in pull-out tests. A few published test results have also been analyzed and explanations given for the variations. Finally, the type of test to be adapted for the estimation of the angle of interfacial friction, depending on the type of reinforced soil structure has been suggested.

## 3. Technique for using fine-grained soil for reinforced earth

With the understanding of mobilization of interfacial friction, an attempt has been made to propose a method by which low-frictional soil can be used as a backfill in reinforced soil structures. It has been shown that, only a small zone of soil around the reinforcement will be actively involved in the mobilization of pull-out resistance. The induced shear stress due to interfacial frictional resistance will distribute rapidly with distance away from reinforcement surface. On this basis, it has been shown that a thin layer of frictional soil around the reinforcement is sufficient while the rest could be of low-frictional soil to get full efficiency (to that of full frictional soil) and this technique has been termed as 'sandwich technique'. By equating the frictional force on reinforcement surface and frictional strength of low-frictional soil at the interface, the optimum thickness of frictional soil has been arrived. Six series of pull-out tests have been carried out with different types of reinforcements, to bring out the effect of thickness of sand (frictional material) around the reinforcement on pull-out resistance. Saw dust and kaolin clay have been used as low-frictional material. It has been concluded that, using sandwich technique, reinforced soil structures can be built with soft and expansive soils using only a minimum amount of frictional soil. However, the excessive deformation of the bulk soft and expansive soils has to be taken care by adapting suitable construction technique.

## 4. Reinforced earth mattress on expansive soil

From theoretical considerations, it has been shown that the surface-loaded footing on expansion soil will reach limit equilibrium condition (factor of safety = 1) upon saturation. By providing a reinforced soil bed

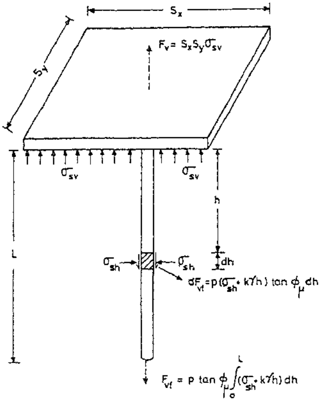

FIG 1. Mechanism of control of heave.

on expansive soil, the performance of loaded footing can be improved. The above aspect has been verified through model tests on expansive soil. A parametric study has been made through plate load tests to delineate the factors influencing the load-carrying capacity of reinforced soil bed on soft and expansive soils. A method has been formulated to predict the load-settlement behavior of the two-layer system, using the load-settlement curves of each of the materials in their semi-infinite state. The available method of analysis has been modified to estimate the improvement in load-carrying capacity. It has been concluded that the stability of the structure resting on soft and expansive soils can be improved with the adoption of reinforced soil technique.

### 5. Control of heave through reinforced earth technique

A method of controlling the heave of the expansive soil through reinforced soil principle has been examined. The frictional resistance mobilized by a reinforcement in vertical position due to horizontal swelling pressure of soil will resist the upward movement of a plate resting on the soil, if it is firmly fastened to the reinforcement, upon inundation (Fig. 1). Theoretically an equation for the heave of a semi-infinite homogeneous expansive soil upon saturation has been derived. From the basic considerations, it has been shown that the length of reinforcement required to control heave is independent of swelling pressure of the soil but dependent on interfacial frictional resistance and sizes of the top plate and reinforcement. To verify this approach three series of tests, *viz.*, laboratory small scale, laboratory moderate scale and field tests have been carried out. The parameters examined in these tests are type, surface characteristics, length, number, placing condition and shape of the reinforcements, thickness of expansive soil layer and size of the top plate. Experimental results have been evaluated in relation to the theoretical values predicted. These test results have indicated the validity of this technique to control heave.

### References

| | |
|---|---|
| 1 JEWELL, R. A. AND WROTH, C. P. | Direct shear tests on reinforced sand, *Geotechnique*, 1987, 37, 53–68. |
| 2. JONES, C. J. F. P. | *Earth reinforcement and soil structures*, Butterworths Advanced Series in Geotechnical Engineering, 1985, Butterworths. |
| 3. VIDAL, H. | The development and future of reinforced earth, *Proc. Symp. Earth Reinforcement*, ASCE, Pittsburgh, 1978, pp. 1–16. |

Thesis Abstract (M.Sc. (Engng))

## **Experimental investigation of fluidically controlled oscillating jet** by T. Srinivas

Research supervisors: B. Vasudevan and A. Prabhu
Department: Aerospace Engineering

### 1. Introduction

Enhanced jet turbulence is desired for improving mixing of the primary jet with the secondary flow in many applications like thrust-augmenting ejectors, fuel injectors, foam-producing devices for fire suppression, etc. Recent experiments[1-3] have shown that apart from hypermixing nozzles and pulsation, oscillation or excitation of the primary jet can also result in enhanced mixing. Various techniques like vane excitation, acoustic excitation and fluidic excitation have been employed in the recent past[3-5] to excite or oscillate the primary jet. Fluidic excitation seems to be promising for practical applications in being self-excited, having no moving parts and by being able to oscillate jets issuing into a different medium. Devices making use of fluidic excitation are basically bistable, the modes being switched by feedback techniques resulting in jet oscillations of large amplitudes.

In this paper, results of a study of a two-dimensional fluidically excited oscillating jet are presented. This study is being carried out with a view to evaluate the performance of a fluidically excited oscillating jet as a spreading, entraining and mixing mechanism. The flow inside the nozzle, the mechanism of feedback resulting in jet oscillation and the influence of nozzle parameters on the frequency of jet oscillation are discussed. The nozzle configuration chosen here produces very large spread angles. However, from the entrainment point of view the oscillating jet seems to be no better than a steady jet.

### 2. Experimental set-up and instrumentation

The basic jet facility was a rectangular nozzle of width 23·8 mm and span 300 mm. Air from a blower was diffused into the long-settling chamber and then accelerated through a contraction (ratio 28) into the fluidic nozzle (Fig. 1). Side plates were used downstream of the nozzle to avoid the lateral spread of the

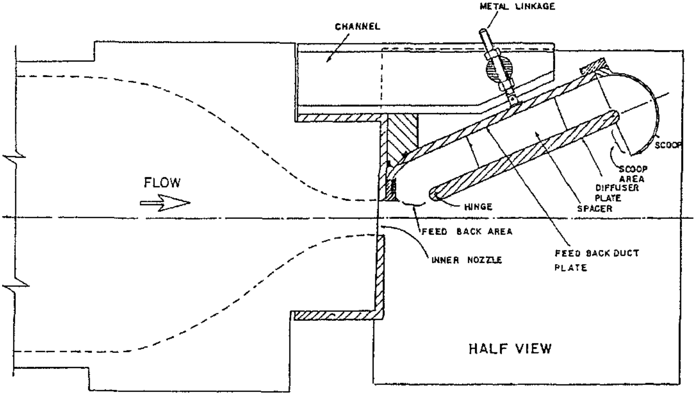

FIG. 1. Feedback nozzle with variable parameters.

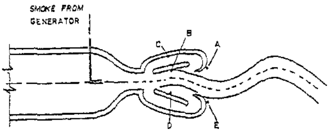

FIG. 2 Schematic of flow pattern frozen by stroboscope.

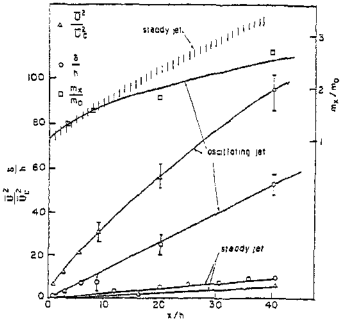

FIG. 3. Development of jet width, centre line velocity and entrainment with x.

jet. The nozzle is designed so that important parameters like nozzle-diffuser angle, the scoop area and the feedback volume can be varied independent of each other.

Pressure and velocities were measured using pitot tube, monometers, Barocell pressure transducer and constant temperature hotwire anemometer. Flow visualisation was carried out using smoke.

### 3. Results and discussion

The flow inside the nozzle was initially visualised by strobing a stream of smoke injected in the contraction, upstream of the throat. The schematic of the flow thus seen in one of the bistable modes, frozen by a stroboscope, is shown in Fig. 2. It shows that the jet is attached to wall B of the diffuser but detaches from this wall upstream of the scoop and then gets attached to the opposite lip E as it issues out of the nozzle. In the other stable mode the flow is a mirror reflection of that shown. This feature of the flow is contrary to that proposed by Viets[6], in whose view the flow remains attached to the wall all along and issues out of the nozzle attached to the lip on the same side. The mode as in Fig. 2 was also confirmed by making and observing the pressure/velocity signals at points A,B,C,D and E simultaneously.

Experiments conducted to evaluate the influence of the parameters on the performance of the oscillating jet showed that the frequency of oscillation is influenced strongly by the velocity of the jet and length of the diffuser wall (feedback length) of the fluidic nozzle. Feedback volume and scoop area did not have appreciable influence. For low-diffuser angles, the oscillation did not occur as the flow would be either fully attached on both the walls or feedback pressure is not sufficient to flip the jet from one wall to the other. For large diffuser angles also the flow did not oscillate since the flow was fully separated from the diffuser wall. In either of these situations the bimodal state could not be established and therefore oscillations did not occur.

The jet development of flow was studied by making average velocity profile measurement at several down-stream stations from the nozzle. Very near the nozzle the profiles showed two peaks in velocity distribution typical of results arising because of bimodal states in the oscillating flow. Far away these peaks were diffused and smoothed out. Figure 3 shows the development of half width $\delta/h$ and inverse square of centre line velocity $U_0^2/U_c^2$. For comparison, values for the steady jet are also shown in the same figure. The variations of $\delta/h$ and $U_0^2/U_c^2$ are linear with distance as it should be for a 2D jet. However, growth rate of $\delta/h$ is very large compared to a steady jet. The large growth or spread rate of the jet (much larger than even the diffuser angle) is due to the new mode of oscillation observed here and also prossibly aided by Coanda effect at the lips. However, the entrainment computed from the developments of the oscillating jet (Fig. 3) shows no improvement compared to a steady jet.

### 4. Conclusion

The flow inside the fluidic nozzle when the jet is oscillating and also the mechanism of pressure build up in the feedback chamber are different from what has been proposed earlier. The main features of oscillating flow have been established. The effect of nozzle parameters on the frequency of oscillation have been described. Even though the fluidic nozzle provides a large jet spread, entrainment is lower than in a steady jet. Thus, the fluidic nozzle seems to be more a spreading device than an entraining one.

### References

1. Bremhorst, K. and Harch, W H — Near-field velocity measurements in a fully pulsed subsonic air jet, *Symp on Turbulent Shear Flows*, Pennsylvania State University, April 1977
2. Simmons, J. M., Platzer, M F and Smith, T. C. — Velocity measurements in an oscillating plane jet issuing into a moving airstream, *J Fluid Mech.*, 1971, **84**, 33–53.
3. Simmons, J. M , Lai, J. C. S and Platzer, M F. — Jet excitation by an oscillating vane, *AIAA J.*, 1981, **19**, 673–676.
4. Crow, S. C. and Champagne, F. H. — Orderly structure in jet turbulence, *J Fluid Mech.*, 1971, **48**, 547–591.
5. Viets, H. — Flip-flop jet nozzle, *AIAA J.*, 1975, **13**, 1375–1379.
6. Viets, H., Balster, D and Thomas, H L. Jr — Feasibility study of unsteady foam generators DOD Aircraft ground fire suppression and rescue office, ARL Wright Patterson Aircraft Base, Ohio, USA.

## Thesis Abstract (Ph.D.)

### **Dynamics and control of flexible spacecraft** by A. G. Sreenatha
Research supervisors: S. K. Shrivastava and M. Seetharama Bhat
Department: Aerospace Engineering

### 1. Introduction

With the advent of large light-weight space structures, structural flexibility of a satellite as a whole, or its components, has become an important factor in the design and analysis of the attitude control systems. Significant research is going in the direction of dynamics and control of large space structures (LSS). Still, many of the present and future generation of satellites can be modelled as the ones having a central rigid body with flexible appendages. Examples of such satellites are the Indian Remote Sensing Satellite (IRS), Solar Electric Propulsion Spacecraft (SEPS), Indian National Satellite (INSAT), INTELSAT, OLYMPUS, to name a few. High-accuracy attitude control of these satellites is necessary so as to meet the stringent mission requirements. The structural vibrations of the appendages affect the accuracy and stability of the controlled attitude motion. Sometimes digitization of sensor output and the method of implementation of control logic can also add to inaccuracy. The present work deals with the analysis of the dynamics and control of such satellites. Possible solutions to overcome the problems are also suggested. The model of the spacecraft considered consists of a central rigid body to which two sun-tracking solar panels are attached along with the pitch axis. Three sensors are assumed to be mounted on the rigid body to measure the roll, pitch and yaw attitude angles. Three reaction wheels, along the principal axes are assumed to provide control torques.

### 2. PWPFM Controller

The initial part of the study deals with the attitude dynamics and problems of control–structure interactions in an Earth-imaging spacecraft. The equations governing the attitude and flexural dynamics are formulated using Newton–Euler and Lagrangian approaches. A conventional pulse–width–pulse–frequency–modular (PWPFM) controller is employed. The PWPFM logic is realized using the Schmitt trigger along with the compensators. This is basically nonlinear due to the presence of the Schmitt trigger The performance of the attitude controller is studied numerically using the complete set of nonlinear equations of motion. The parameters for the simulation study correspond to those of IRS. The damping generated using the pseudo-rate modulator (PWPFM) is found to be insufficient. Hence, a twelfth-order Kalman Filter is employed to estimate the attitude angles and their rates. The additional feedback of angular rates is used to improve the damping. For remote-sensing satellites, the attitude and body rate specifications are very stringent. Digital sensor characteristics like sampling and quantization may affect the performance adversely. The simulation study shows that these effects are more prominent than the effects of flexibility for the satellite selected.

### 3. Digital controller

The conventional practice is to first design an analog controller, and then implement it in the digital form. However, such a scheme has many drawbacks. The abundance of modern computers and the advances in microprocessor technology provide further motivation for the direct design of the controller in digital form. The remaining part of the dissertation deals with the design of a digital controller for a flexible spacecraft.

The linear quadratic Gaussian (LQG) theory is employed frequently for design of a controller because: 1) the resulting controller is analytically derivable, and 2) it yields a stable closed-loop system. The necessity of an estimator, of nearly full order as the system for estimating the states from limited measurements makes it prohibitive from the point of view of implementation. On the other hand, the use of output feedback alone may not provide the required stability and performance characteristics. Hence, a lower order output feedback dynamic controller may be envisaged which overcomes the aforesaid difficulties. The order of the dynamic controller is basically decided by its stabilizing property of the closed-loop system. The latter part of this study deals with the design of an optimal, low-order dynamic controller for a flexible spacecraft of the type of SEPS[1].

The equations governing the speecraft dynamics in discrete form can be written as,

$$\mathrm{x}_{k+1} = \mathrm{Ax}_k + \mathrm{Bu}_k + \mathrm{Gv}_k$$
$$\mathrm{y}_k = \mathrm{Cx}_k + \mathrm{H}w_k$$

where A, B and C represent the system matrices, and G and H, the state and measurement noise matrices. The order of the system is $n$ with $m$ inputs and $l$ outputs. $\mathrm{v}_k$ and $\mathrm{w}_k$ are stationary, zero-mean, stochastic vectors. It is intended to design an r-dimensional time-invariant controller described by,

$$\mathrm{z}_{k+1} = \mathrm{Dz}_k + My_k$$
$$\mathrm{u}_k = Nz_k + \mathrm{Ky}_k.$$

The design problem is to find the optimal values for the matrices D, M, N, and K such that the expected quadratic cost,

$$J = E\,\Sigma\,(\mathbf{x}_k'\,\mathbf{Q}\mathbf{x}_k + \mathbf{u}_k'\,\mathbf{R}\mathbf{u}_k)$$

is minimized. The design problem is reset into a pure output feedback problem by augmenting the controller states with the plant states. The necessary conditions leading to optimality are given. The basic difficulty in the design of a low-order controller is to find a stabilizing feedback matrix for initializing the optimization algorithm. A systematic way of choosing elements of the feedback matrix, based on the digital form of the PD controller, is proposed.

Next, the robustness of the digital controller is enhanced by incorporating a prescribed degree of stability in the design by making use of the concept of alpha-shift[2]. A novel method of block-shift is introduced to move different sets of closed-loop eigenvalues by different amounts. Design of a third-order controller for an eighteenth-order system is presented. Improvement in the satellite attitude response with block-shift is demonstrated through numerical simulations. The advantages of this block-shift include: 1) improvement in the system response, 2) greater robustness to the parameter variations on the dominant motion through increased alpha-shift to the corresponding eigenvalues than the simple uniform alpha-shift.

### 4. Digital servo-system

Finally, the design of a robust feedback–feedforward controller for tracking constant reference inputs in the presence of sensor and actuator noises is taken up. The feedback controller is a low-order dynamic controller. The design of the feedback–feedforward controller is carried out using LQG technique. The design problem is reset into an output feedback problem and then the optimal gains are obtained. The robustness of the controller is enhanced using the block-shift concept. The block-shift is shown to improve the tracking considerably. Response curves are obtained for SEPS with a third-order feedback–feedforward controller. Such a controller will come in handy for on-orbit maneuvering. Finally, the nonlinear equations in continuous domain are simulated along with the digital controller. The response curves for attitude and rate response are generated to understand the dynamical behaviour.

### 5. Concluding remarks

This study deals with the design and analysis of a digital, optimal low-order controller for a flexible spacecraft using LQG technique. First, a conventional PWPFM controller is employed to understand the effects of digitization (quantization and sampling). Noting that these effects are quite significant, direct design of the controller in the digital domain is attempted. A block-shift method is suggested for differential shifting of the closed-loop eigenvalues Numerical simulations are carried out to validate the controller.

### References

| | |
|---|---|
| 1 Sreenatha, A G<br>Seetharama Bhat, M<br>and Shrivastava, S K | An optimal dynamic output feedback controller for a flexible spacecraft, *J. Optimal Control Applic. Meth.*, 1990, **11**, 51–66. |
| 2. Seetharama Bhat, M<br>Sreenatha, A. G and<br>Srivastava, S K | Robust low-order dynamic controller for flexible spacecraft, *IEE Proc.–D*, 1991, **138**, 460–468 |

## Thesis Abstract (Ph.D.)

## **Study of some thermal design problems in high-density SMT/hybrid micro-circuit assemblies** by S. Ramamohan Rao

Research supervisors: M. Satyam, K. Ramakumar and V. P. Kulkarni
Department: Electrical Communication Engineering

### 1. Introduction

One of the main factors contributing to the reliable performance of high-density surface-mounting technology (SMT)/hybrid micro-circuit assemblies, used in space/military/computer fields, is thermal design. Methods used by some investigators[1–4], particularly in earlier investigations, are more empirical in nature and mostly involved simple mathematical formulations like graphical techniques for obtaining temperature distributions, etc. Computer-aided design (CAD) tools are used for more rigorous modelling and these models are rather complex and call for elaborate mathematical techniques. It is seen from the previous investigations that the emphasis is mainly on mathematical techniques like Fourier Transforms or special mathematical procedures for pins/packages or new substrate materials or simple thermal analysis, etc.

### 2. Program of work

From the previous work it may be seen that these investigations did not take into account the possibility of locating thermally sensistive devices (TSD) in better and safe operating areas of the circuit substrate. Further, in dense circuit layouts the effects of neighbouring components is not studied systematically.

In this program, an attempt has been made to arrive at design guidelines to locate TSD in safe areas. This has been possible through the study of temperature distributions using finite difference methods

(FDM) under various conditions of heat sources, their locations and thermal loading through passive components on different substrate materials.

### 3. Results

In the studies/simulations it is assumed that the boundaries are maintained at a constant reference temperature. The effect of various parameters involved in arriving at the optimal locations of the TSD and selecting the neighbouring components is found as follows.

*Substrate thermal conductivity*: Low thermal conductivity substrate results in maximum temperature in the devices.

*Substrate area:* The more the substrate area, more is the temperature in the device for the constant temperature at the edges of the substrates.

*Area of the heat source:* The more the area of the heat source, the less is the temperature and can be concluded that the minimum amount of area of contact with the substrate is to be ensured to avoid hot spots.

*Location of add-on components:* The location of add-on component can be felt if the add on component is within 10% of semi-diagonal distance (length) of the substrate.

*Distance between two heat sources*: Adverse effects in rising the temperature is rather more, if the two heat sources are located within 10% of the semi-diagonal distance.

*Multiple heat sources and multiple add-on components:* The hot spots can be felt if the add on component is within 10% of the semi-diagonal distance and placing thermally conductive component regions in certain specific locations.

*Sensitivity analysis and location of TSD:* The variation in temperature at different points of the substrate with variations in heat power of one or more heat sources is carried out which enables to find the safe areas for the location of TSD.

Appropriate programmes have been developed using finite difference method (FDM) techniques on CDC–170/180 computer system to carry out the simulation studies.

### 4. Conclusion

This study attempts to arrive at simple thermal design principles for avoiding hot spots and locating TSDs in high-density SMT/hybrid micro-circuit assemblies. A few typical thermal design simulations have been given with various parameters involved and sensitivity analysis and procedures for the location of TSDs are developed. A set of basic thermal design guidelines are generated to reduce the overall design time for layouts and to ensure better thermal performance of such assemblies. This analytical tool may help in generating optimal routing and layout from thermal point of view for high-density SMT/hybrid micro-circuit assemblies in minimum design time.

### References

| | |
|---|---|
| 1. Avaram Bar-Cohen *et al* | Thermal frontiers in the design and packaging of microelectronic equipment, *Mech. Engng*, 1983, **105** (6), 53–59. |
| 2. David, R. F. | Computerized thermal analysis of hybrid circuit, *IEEE Elec. Comp. Conf*, 1977, pp. 324–332. |
| 3. Rodriquiz Corre, M. | Finite difference analysis simplifies heat transfer problems, *Mech. Des.*, Dec. 6, 1984, **56**(28), 128–132. |
| 4. Buchman, R. C and Ruber, M. K. | Thermal considerations in the design of hybrid microelectronic packages, *Solid St. Technol.*, Feb. 1973, **16**(2), 39–43. |

Thesis Abstract (Ph.D.)

## On interruptions, optimal configurations and productivity in a complex production system—Some computer simulation models by Kavuri Suryaprakasa Rao

Research supervisors: K. N. Krishnaswamy, B. G. Raghavendra and V. Ramachandran (Fertilizer Corporation of India Ltd)
Department: Management Studies

### 1. Introduction

One of the major problems faced by operating managers in large process industries is maintaining uninterrupted operation of the production system. However, the reliability of large-scale process industries has often been affected due to design considerations aimed at thermal economy. These industries commonly face the problem of frequent interruptions and consequent loss of productivity. However, the reliability of a plant can be improved by keeping stand-bys for equipment or additional streams to the plant itself.

The decisions involved in these situations generally are assessment of additional features required to improve the system performance and estimating it with the added features. From the available literature[1-5] it appears that these problems have not been attempted so far. The approach taken in this study is one of industry-specific research, with an eye on generalisations. The production system chosen is a large-scale fertilizer complex. A total system study indicated the following issues for investigation:

(a) Finding the effects of changes in the configurations of process plants on the overall system performance to evaluate a proposal for an additional facility to the existing complex.

(b) Identifying the policies to reduce interruptions of the total processing system which is a combination of several plants to improve the operational productivity.

It was envisaged that a composite methodological approach would be taken up to achieve the above objectives. The first part of this methodology would be a micro study to determine the desired/optimal configuration analysing the failure data. The second part would be to estimate the productivity loss and derive policies to prevent these failures to minimize such loss. The essence of the methodology is the linking of the two approaches suitably.

Fertilizer production at the complex being studied is based on coal gasification technology. The complex comprises four interconnected plants, namely, coal gasification, ammonia, steam generation and urea.

### 2. Micro analysis of a process plant

The first objective of the study involves the analysis of a part of the complex, the coal gasification plant. The analysis of failure data led to the conclusion that the operational conditions of the plant at any time period can be viewed as a Markov process. The maximum number of states, $N$, the system can occupy can be obtained from

$$N = \frac{(K+1)(K+2)}{2} \tag{1}$$

where $K$ represents the number of parallel streams of the plant.

The gasification plant has three parallel streams and its state-space consisting of ten possible states was identified. The state of the plant was represented by the number of streams 'running' (r), 'under maintenance' (m) and 'idle' (s) which can be represented by a three subscript variable $S_{rms}$ such that $(r + m + s = K)$. The transition diagram indicating the transitions among the states of the plant is presented in Fig. 1.

The gasification system states and its time of occurrence were derived from the data recorded in plant's log book. From these basic data, transition probability matrix (TPM) was also derived. The long-run performance of the system can be estimated by the steady-state probabilities obtained from the steady-state equations,

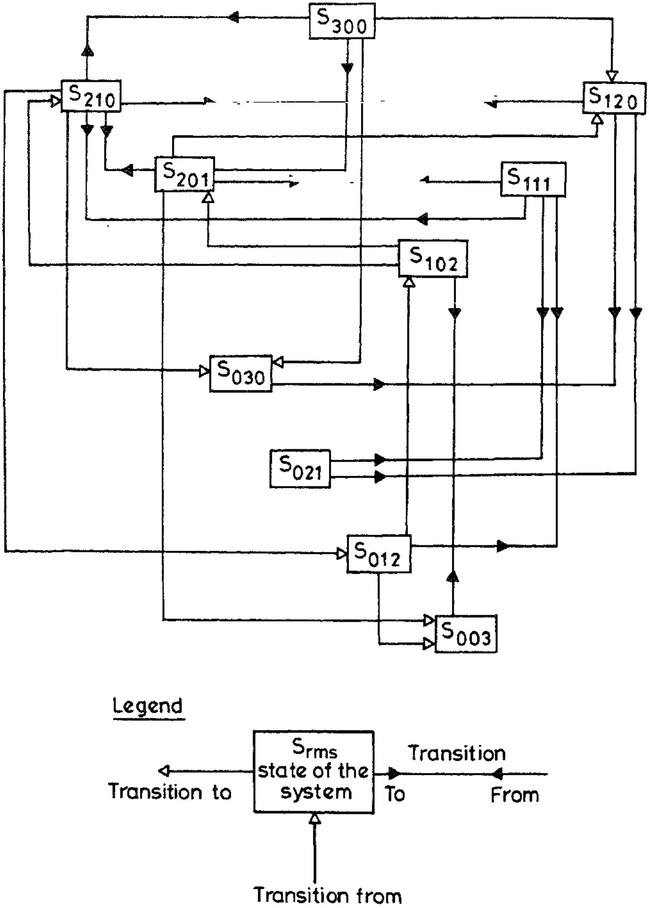

FIG. 1. Transition diagram for three gasifiers system.

$$\Pi = \Pi P \tag{2}$$

and

$$\sum_{j=1}^{N} \Pi_j = 1 \tag{3}$$

where $\Pi$ is the row vector with components $\Pi_i$, the vector of steady-state probabilities, and P, the TPM.

The configurational charges of the gasification plant were observed with reference to waste heat-recovery system of each gasifier. The steady-state probabilities of system states were obtained for each configuration from the solution of the steady-state equations.

To predict the performance of a system with four streams of gasifiers which include the proposed fourth unit, a simulation experiment was designed using Markov model. To do this, it was necessary to develop independent Markov models for each one of the three streams The new system was construed as a combination of a three-unit system and a single unit. All the possible configurations of the system of four streams were identified and each of them was simulated. The results of the Markov simulation were analysed to identify an optimal configuration of the process plant.

An alternative method to the Markov simulation model, a 'Markov model with rewards', was used to estimate analytically the process gain of each configuration of the gasification plant and the results were found to be very close to the ones obtained in the simulation model. An LP model was used to check the adequacy of steam production in the Fertilizer complex taking into consideration the configurational changes of coal gasification plant.

### 3. Macro analysis of industrial processing complex

The second objective of the study is related to the total system performance. The data of production interruptions for the total Fertilizer complex were analysed by developing an 'Interruption tree'. An Interruption tree model (ITM) of the Fertilizer complex is presented in Fig. 2.

The tree consists of various branches, each referring to a particular type of interruption, with its probability of occurrence and contribution to loss of production. The top event in the tree, an interruption to the overall production of urea, points to five blocks, with data available on arrival and duration distributions. Each block represents a major area of interruption, with data available on the estimated probability of occurrence. Each one of these five blocks, in turn, points to further set of nodes, representing the type of interruption within the major area, along with the respective probability of occurrence. The lowest level of events is called basic nodes representing basic causes of interruptions to the production. State of the system can be represented by the notation $(i, j)$, where $i$ stands for block of interruption and $j$ identifies the associated basic node

The interruption tree developed for the Fertilizer complex was used in a simulation model to estimate the performance of the system, the total Fertilizer complex, in terms of effective system availability (ESA), production of urea, and operational productivity of inputs.

Effective system availability was computed using the equation,

$$\mathrm{ESA} = \frac{\sum_{i=1}^{n} \sum_{j=1}^{r_i} d_{ij}(100 - L_{ij})}{\sum_{i=1}^{n} \sum_{j=1}^{r_i} d_{ij}} \tag{4}$$

where $r_i$ is the number of basic nodes for the block $i$, $d_{ij}$, the number of hours the system spent in the state $(i, j)$, and $L_{ij}$, the expected production loss percentage associated with the state $(i, j)$. ESA is expressed as a percentage of effective hours available for operation to the total hours.

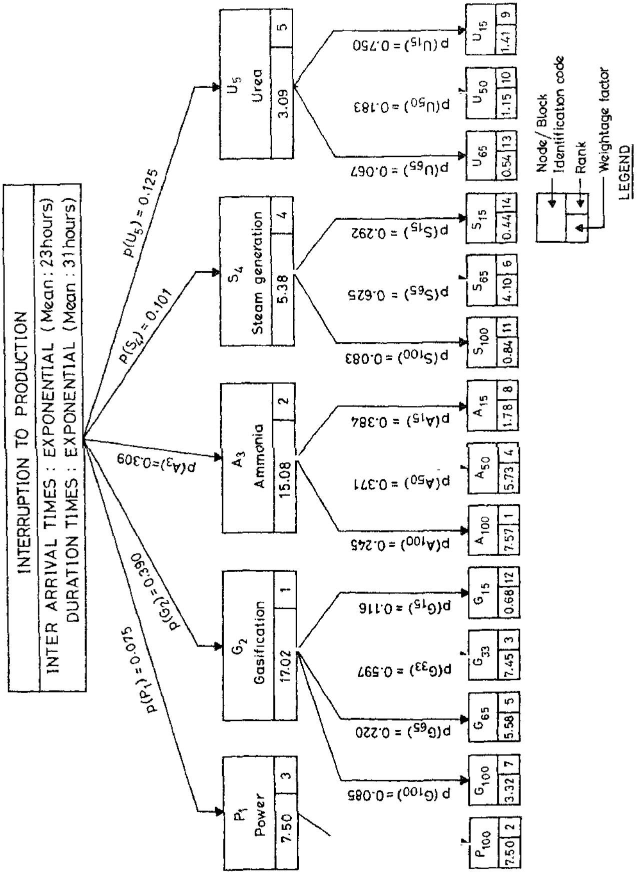

FIG. 2. Interruption tree model for the Fertilizer complex.

Rank of each basic node and block was arrived based on its weightage factor. The weightage factors were computed from the following equations:

$$W_{ij} = \text{weightage factor of basic node } j \text{ in block } i = (p_i\, p_{ij}\, L_{ij}) \quad (5)$$

$$W_i = \text{weightage factor of block } i$$

$$\sum_{j=1}^{r_i} (p_i\, p_{ij}\, L_{ij}) \quad (6)$$

where $p_i$ is the expected probability of occurrence of interruption in block $i$ and $p_{ij}$, the expected probability of occurrence of interruption due to basic node $j$, in the $i$th block

The management concern for productivity gain by reducing the interruptions was reflected in two policies. The policies were aimed at selecting either (i) a scheme of reducing interruptions in the sequence of the ranks of basic nodes, or (ii) a scheme of reducing interruptions in the sequence of the blocks. The interruption tree was simulated under each policy to predict the performance of the system.

### 4. Results and conclusions

Steady-state probabilities obtained from the Markov analysis showed that the performance of each configuration was different. The configuration in which the waste heat-recovery system was bypassed in all the three streams gave the maximum system availability for operation when compared to the other two. The results of the Markov simulation and subsequent analysis indicated as an optimal configuration the four-gasifier system with one of them having the waste heat-recovery provision.

The results of the ITM simulation under each policy were compared to arrive at an optimal policy. It was observed that the productivity loss would be minimum under the first policy, namely, the schemes for reducing interruptions node by node, in the order of ranks associated with them.

The results of Markov simulation model and interruption tree model are of particular interest to the operating manager as they help in making better decisions regarding (i) the selection of optimum configurations of process plants with known failure rates of equipment, (ii) additional investments on plants and equipment, and (iii) fixing operational priorities with reference to maintenance policies of plants and equipment.

A generalised composite methodology which links both the micro and macro models could be applicable to any industrial processing system.

### References

| | |
|---|---|
| 1. Chang, S. and Talbot, G. R. | Dynamic simulation and phase plane analysis of entrained coal gasification, *Simulation*, 1986, **46**, 244–250. |
| 2. Davis, R. P and Kennedy, W. J. | Markovian modeling of manufacturing systems, *Int. J. Prod. Res*, 1987, **25**, 125–132. |
| 3. Malmborg, C. J., Brammer, K. W. and Krishnakumar, B. | A decision support system to evaluate maintenance requirements of recoverable item population, *IEEE Trans*, 1987, **SMC-17**, 465–473. |
| 4. Richardson, K. V. | A Markov chain model for determining resources for industrial processing, *Op. Res. Q.*, 1980, **21**, 119–124. |
| 5. Walsham, G | A computer simulation model applied to design problems of a petrochemical complex, *Op. Res.*, 1975, **21**, 399–410. |

---

## Thesis Abstract (Ph.D.)

## **Resistivity, switching behaviour under pressure and crystallization studies on Al–Te glasses** by R. Ramakrishna

Research supervisors: E. S. Raja Gopal and S. Asokan
Department: Instrumentation and Services Unit

### 1. Introduction

Chalcogenide glassy semiconductors exhibit many interesting electrical properties including the pheno-

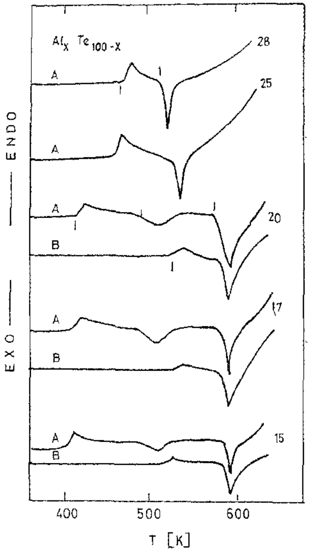

FIG. 1. Differential calorimetric traces of $Al_xTe_{100-x}$ glasses; heating rate 15 K/min.

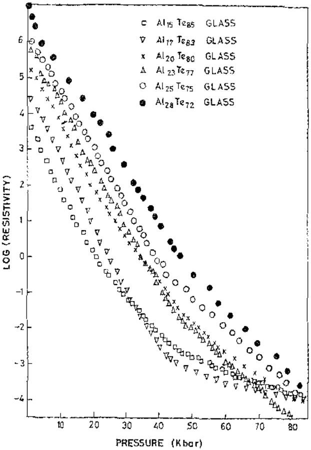

FIG. 2. The variation of electrical resistivity of $Al_xTe_{100-x}$ glasses with pressure.

menon of switching[1]. Electrical switching is reversible (threshold) or irreversible (memory) depending on the stability of the glass against devitrification[1]. The study of the behaviour of glasses under external influences like temperature, pressure, etc., will be helpful in understanding its stability and suitability for particular switching application. The present work involves the study of high pressure and thermal behaviour of $Al_xTe_{100-x}$ glasses of different compositions ($15 \leq x \leq 28$). The effect of pressure on the memory switching of Al–Te glasses has also been undertaken.

## 2. Experimental

Bulk $Al_xTe_{100-x}$ glasses ($15 \leq x \leq 28$) have been prepared by melt quenching. Electrical resistivity under pressure, at ambient and at low temperatures (down to 77 K), has been studied using a Bridgman anvil system, developed and fabricated in our laboratory. Thermal crystallization behaviour of $Al_xTe_{100-x}$ glasses ($15 \leq x \leq 28$) has been studied using a Stanton–Redcroft differential scanning calorimeter. The electrical switching behaviour of these has been investigated using a PC-based system specially developed for this purpose.

## 3. Results and discussion

Differential scanning calorimetric studies indicate $Al_xTe_{100-x}$ glasses with $15 \leq x \leq 23$ exhibit a double glass

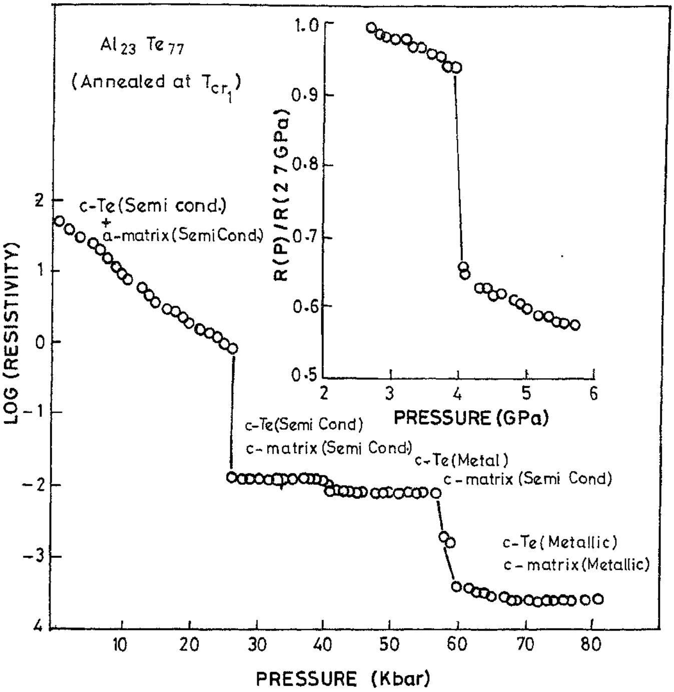

FIG. 3. Pressure dependence of electrical resistivity of $Al_{23}Te_{77}$ glasses annealed at the first crystallization temperature.

transition and double-stage crystallization, whereas glasses with x > 23 show only a single glass transition and single-stage crystallization (Fig. 1). The first crystallization reaction in $Al_xTe_{100-x}$ glasses with $x \leqslant 23$ corresponds to the precipitation of hexagonal Te in a residual Al-rich amorphous matrix. The second reaction corresponds to crystallization of the matrix. Further, the complete crystallization of Al-Te glasses leads to the formation of a new Al-rich phase, $\phi$ (Al–Te), which is not the equilibrium crystalline phase of the system[2]. The composition of crossover in the crystallization behaviour can be connected with a phenomenon known as 'rigidity percolation'[3-5].

Electrical resistivity measurements under pressure indicate that all the $Al_xTe_{100-x}$ glasses exhibit a continuous decrease in the electrical resistivity and activation energy for electrical conduction under pressure, with the samples becoming metallic at high pressures around 70–80 k bar (Fig. 2). Continuous semiconductor-metal transition of Al–Te glasses can be due to a continuous closure of band gap which is a common feature in materials exhibiting continuous metallization. High-pressure metallic phases of Al–Te glasses are also found to be crystalline.

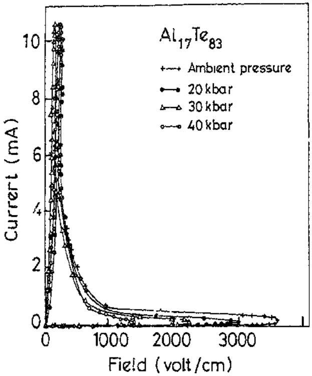

FIG. 4. Electrical switching characteristics of $Al_{17}Te_{83}$ glasses at different pressures.

High-pressure resistivity measurements have also been undertaken on a representative $Al_{23}Te_{77}$ glass, annealed at the first and the second crystallization temperatures. $Al_{23}Te_{77}$ glass, annealed at the first crystallization temperature, is found to exhibit three transitions in electrical resistivity. The transitions are identified to be the discontinuous crystallization of Al–Te matrix, the semicoinductor to metal transitions of the precipitated crystalline Te and the Al–Te matrix, respectively (Fig. 3). $Al_{23}Te_{77}$ samples annealed at the second crystallization temperature show a transition corresponding to the discontinuous metallization of the Al-rich crystalline matrix present in the material.

The study of I–V characteristics and electrical switching behaviour at different pressures has been carried out on two representative glasses, $Al_{17}Te_{83}$ and $Al_{20}Te_{80}$. It is found that these glasses show a current-controlled negative resistance behaviour with memory above a critical field $E(t)$ (Fig. 4). The threshold field $E(t)$ of both the glasses is found to decrease linearly with pressure. As the threshold field depends on the initial resistivity of the samples, the decrease in resistivity with pressure explains the decrease of $E(t)$ with pressure.

## References

| | |
|---|---|
| 1. ZALLEN, R. | *The physics of amorphous solids*, 1983, Wiley. |
| 2. RAMAKRISHNA, R., ASOKAN, S., PARTHASARATHY, G., TITUS, S. S. K. AND GOPAL, E. S. R. | Calorimetric studies of Al–Te glasses: Composition dependence of crystallization and a new compound in the Al–Te system, *J. Non-Crystalline Solids*, 1992, **139**, 129–136. |
| 3. PHILLIPS, J. C. | Vibrational thresholds near critical average coordination in alloy network glasses, *Phys. Rev. B*, 1985, **31**, 8157–8163. |
| 4. PHILIPS, J. C. AND THORPE, M. F. | Constraint theory, vector percolation and glass formation, *Solid St. Commun.*, 1985, **53**, 699–702. |
| 5. ASOKAN, S., PRASAD, M. V. N., PARTHASARATHY, G. AND GOPAL, E. S. R. | Mechanical and chemical thresholds in IV–VI chalcogenide glasses, *Phys. Rev. Lett.*, 1989, **62**, 808–810 |

Thesis Abstract (M.Sc. (Engng))

## **Corrosion behaviour of equiatomic nickel–titanium alloy in 3.5% NaCl, 89% conc. $H_3PO_4$ and extracellular biofluids** by S. Muzhumathi

Research supervisors: D. H. Sastry and K. I. Vasu
Department: Metallurgy

### 1. Introduction

Surgical inplants such as bone fixation plates, hip nails, Harrington distraction rods, etc., are widely being used. Stainless steel (mainly 316 L type) and titanium alloys (especially Ti–6Al–4V) are the usual choice for such applications. However, a major problem with these implant materials is the failure due to corrosion. There is therefore a need to develop new and better prosthetic materials. A possible candidate material for prosthetic applications is the equiatomic nickel–titanium (NiTi) alloy[1–3]. This alloy exhibits shape-memory effect at the body temperature which helps in its perfect accommodation to the required shape However, the corrosion properties of this alloy, particularly in biofluids, are not available in literature. The present study aims at filling this need. Investigations are undertaken with reference to general corrosion, pitting corrosion and corrosion in biological fluids.

### 2. Experimental

The intermetallic compound NiTi was prepared by arc-melting in argon atmosphere. The alloy was melted thrice to achieve good homogeneity and was further homogenised by heating at 1123 K for 4 h. Homogenisation at 1373 K (for 24 h) led to eutectoidal decomposition forming $NiTi_2$ and $Ni_3T_1$. Attention in this work was, however, paid to only the single-phase (NiTi) alloy but not to the two-phase ($NiTi_2$ + $Ni_3Ti$) alloy. The chemical composition was analysed by EPMA and oxygen and hydrogen were analysed in a gas analyser. Microhardness measurements showed that the homogenised alloy was harder than 316 L steel.

Corrosion studies were made on the as-cast (dendritic microstructure) as well as heat-treated (equiaxed grain structure) NiTi in (i) 3.5% sodium chloride solution, (ii) conc. phosphoric acid solution, and (iii) extracellular biofluid. The open circuit potential variation with respect to time was monitored continuously for 24 h. The potential variations were measured with respect to reference-saturated calomel electrode. In extracellular biofluids, the potential *vs* time variations were measured for both NiTi and the common surgical implant material 316L SS. Anodic and cathodic polarisation curves were recorded in x-y recorder. AC impedance studies were also carried out.

### 3. Results and conclusions

With the high-current argon arc-melting technique employed here, it was possible to produce NiTi alloy with almost complete elimination of porosity, microsegregation and volatile matter. The dissolved gases also showed a drastic decrease—the oxygen content in the alloy was about 200 ppm as against 600 ppm in nickel and 2000 ppm in titanium and hydrogen was about 5 ppm as against 33 and 10 ppm in nickel and titanium, respectively.

Polarisation curves have indicated that the rate of both anodic and cathodic reactions follows Tafel behaviour, *i.e.*,

$$E = a + b \log i_c$$

where $E$ is the electrode potential of the specimen, $i_c$, the current density of the electrochemical reaction and $a$ and $b$ are constants (Table I).

Broadly, similar results are obtained in phosphoric acid solution. In NaCl solution, the alloy shows no propensity to pitting at applied potential of 2000 mV; the pitting potential $E_p$ is more noble than $E_c$, the corrosion potential. However, a mild tendency for pitting is noticed in phosphoric acid.

A comparative study is made of the corrosion behaviour of commercially available surgical implant

**Table I**

**Corrosion parameters for heat-treated and as-cast NiTi in 3·5% NaCl**

| *Condition of alloy* | *Corrosion potential mV/SCE* | *Tafel slope/decade* | | *Current density μA/cm²* |
|---|---|---|---|---|
| | | *a* | *b* | |
| as-cast | −0·293 | 0·074 | 0·119 | 5·03 × $10^2$ |
| heat-treated | −0·446 | 0·082 | 0·192 | 1·14 × $10^2$ |

material 316L stainless steel and NiTi in extracellular body fluid. The potential *vs* time curves for stainless steel show that the potential is more positive, the same being more negative for NiTi. The corrosion current density for SS and NiTi are 0·86 and 0.39 mA/cm², respectively; the corrosion rate of SS is about twice that of NiTi. Furthermore, NiTi has a higher microhardness value than 316L SS. Both materials were immersed in extracellular biofluids for one month and later analysed by scanning electron microscopy for pit size and distribution. 316L SS has shown larger pit dimension and higher pit density compared to NiTi.

The study has shown that NiTi has good resistance to corrosion in NaCl and phosphoric acid solutions. In extracellular biofluids, its corrosion resistance is far superior to that of 316L stainless steel. Hence, NiTi is quite suitable for implant applications.

### References

1. Wagner, H. J. and Jackson, C. M. *Mater. Engng*, 1969, **70**, 28.
2. Otsuka, K. and Shimizu, K. *Int. Matals Rev.*, 1986, **31**, 93–114.
3. Sekiguchi, Y., Dohi, T. and Funakubo, H. *Proc. 8th Annual Meeting of Society of Biomaterials*, Orlando, USA, 1982, p 92, Society of Biomaterials.

---

## Thesis Abstract (M.Sc. (Engng))

## **Influence of welding conditions on bead characteristics in flux-cored arc welding** by V. Balraj

Research supervisors: K. S. S. Murthy and K. L. Rohira (BHEL)
Department: Mechanical Engineering

### 1. Introduction

Weld quality and soundness depend on the final bead shape and the eventual bead shape assumed by a weld depends upon the distribution of energy input from the arc, fluid flow patterns within the weld pool, heat flow from the weld pool and capillary phenomenon, etc.[1,2]. The surface profile and dimensions of the deposited weld metal and the meniscus formation are very important in the groove joints as they govern the stress concentration potential[3].

The geometry of the joint is determined by welding conditions and thermophysical properties of the materials to be welded. In flux-cored arc welding interfacial tension forces play a significant role on the bead shape formation as the slag phase also exists in this process[4]. Also, the molten flux reacts with molten metal and alters the weld metal chemistry and in turn the mechanical properties of the weld metal[5].

### 2. Experimental work

In this work, the bead shape formation in the first pass in V groove has been studied by measuring wetting angle, penetration angle, deposited bead height, the profile of reinforcement and meniscus. Particular emphasis is laid on studying the influence of shielding gas composition, welding current and V-groove angle effects on interfacial tension forces which in turn influence the bead morphology A mathematical model based on interfacial tension forces has also been developed. Influence of shielding has and slag on weld metal chemistry also gas been studied.

Flux-cored arc welding trials were conducted using 20mm thick plates of boiler quality carbon steel material, wherein V grooves of angles ranging from 60 to 120 were machined. Shielding gas with varying compositions of carbon dioxide with argon and basic and rutile wires of 1·6 mm dia size were used. All the experiments were carried out at a constant welding speed of 5 mm/s at 250, 300 and 350 A current levels.

### 3. Results and discussion

The results show that the desirable flat bead surface in V grooves is possible at lower currents and lower carbon dioxide gas composition with rutile wire and at a higher current, higher carbon dioxide gas composition with basic wire. Based on the above results, a regional diagram has been developed which can be directly used to select the welding conditions under which the desirable bead surface can be obtained At higher welding currents, the influence of interfacial tension forces are not significant due to higher temperature fields and thermal activity of the flux and the bead morphology is governed only by the electromagnetic force.

Ripple formation on the bead surface was observed while using the basic type wire. This could be attributed to higher viscosity of the molten flux of basic type wire. Increase in carbon dioxide content in the shielding gas mixture increases the penetration angle, interfacial tension forces and decreases the wetting angle. With basic type wire, meniscus formation at the edges was observed which can lead to undercuts. This may be due to lower fluidity of the molten flux and higher cohesive force between molten flux and solid metal. The increase in depth-to-width ratio with relative values of interfacial tension forces confirms the influence of these forces on penetration. A mathematical model has been developed based on interfacial tension forces. From the evaluation of the model, it has been found that the contribution of electromagnetic force to the formation of the bead reinforcement area is 40 to 50% higher compared to the contribution of interfacial tension and hydrostatic forces. A mathematical model[6] has been modified to predict the bead characteristics based on interfacial tension force wherein the characteristics of flux-cored arc welding process have been incorporated.

The thermochemical reaction of the gas and slag is significant with rutile wire both at droplet and weld pool stages compared to basic wire. The oxygen, generated by the breakdown of carbon dioxide and oxide through melting of flux, promotes humping in most of the weldments of basic wire. The oxygen generated promotes humping in most of the weldments of basic wire. Though oxygen in the weld metal is more with rutile wire, the physical properties of the molten flux promote most of the weld bead flat with good wettability. The increased oxygen content as a result of increased carbon dioxide content in the shielding gas increases penetration by influencing electron emission. At higher currents, the influence of oxygen content on penetration is insignificant. The oxidation of carbon is higher in the weld metal using rutile wire which will affect the mechanical properties. The elements transferred from the flux increase the hardness of the weld metal in rutile wire weld beads and the heat-affected zone (HAZ) hardness is also higher compared to basic wire. The results will be useful in the selection of proper welding conditions under which a quality weld bead can be obtained.

### References

1. Shultz, B L and Jackson, C. E. Influence of weld bead area on weld metal mechanical properties, *Weld. J.*, 1973, **52**, 26s–37s.

2. Schemmer, D. D., Olson, D. L. Williamson, D L. The relationship of weld penetration to the welding flux, *Weld. J.*, 1979, 153s–160s.

3. BRADSHEET, B. J *et al* Effect of surface tension and metal flow on weld bead formation, *Weld. J.*, 1968, 47, 314s–322s.

4. REINHART, T. L *et al* The influence of ionic character on welding flux behaviour, *Int. Conf. on Welding Res. in the 1980s*, Japan Welding Research Institute, Osaka, Japan, October 1980

5. MEYENDORF, N *et al* Metal gas reactions in gas shielded arc welding, *Weld Int*, 1988, **2**, 653–657.

6. NISHIGUCHI, K *et al* *Study on bead surface profile*, IIW.Doc 212–392–77